CONNECTING TRANSITIONS IN GALAXY PROPERTIES TO REFUELING

Sheila J. Kannappan[1], David V. Stark[1], Kathleen D. Eckert[1], Amanda J. Moffett[1], Lisa H. Wei[2,3], D. J. Pisano[4,12], Andrew J. Baker[5], Stuart N. Vogel[6], Daniel G. Fabricant[2], Seppo Laine[7], Mark A. Norris[1,8], Shardha Jogee[9], Natasha Lepore[10], Loren E. Hough[11], and Jennifer Weinberg-Wolf[1]

[1] Department of Physics and Astronomy, University of North Carolina, 290 Phillips Hall CB 3255, Chapel Hill, NC 27599, USA; sheila@physics.unc.edu
[2] Harvard-Smithsonian Center for Astrophysics, 60 Garden Street MS-20, Cambridge, MA 02138, USA
[3] Atmospheric and Environmental Research, 131 Hartwell Avenue, Lexington, MA 02421, USA
[4] Department of Physics, West Virginia University, P.O. Box 6315, Morgantown, WV 26506, USA
[5] Department of Physics and Astronomy, Rutgers, the State University of New Jersey, 136 Frelinghuysen Road, Piscataway, NJ 08854-8019, USA
[6] Department of Astronomy, University of Maryland, College Park, MD 20742-2421, USA
[7] Spitzer Science Center, Caltech, MS 220-6, Pasadena, CA 91125, USA
[8] Max Planck Institut fur Astronomie, Konigstuhl 17, D-69117, Heidelberg, Germany
[9] Department of Astronomy, University of Texas at Austin, Austin, TX 78712, USA
[10] Department of Radiology, University of Southern California and Children's Hospital Los Angeles, 4650 W Sunset Boulevard, MS#81, Los Angeles, CA 90027, USA
[11] Department of Physics, University of Colorado at Boulder, Boulder, CO 80309-0390, USA
Received 2012 August 8; accepted 2013 July 17; published 2013 October 15

ABSTRACT

We relate transitions in galaxy structure and gas content to refueling, here defined to include both the external gas accretion and the internal gas processing needed to renew reservoirs for star formation. We analyze two $z = 0$ data sets: a high-quality $\sim$200 galaxy sample (the Nearby Field Galaxy Survey, data release herein) and a volume-limited $\sim$3000 galaxy sample with reprocessed archival data. Both reach down to baryonic masses $\sim10^9$ $M_\odot$ and span void-to-cluster environments. Two mass-dependent transitions are evident: (1) below the "gas-richness threshold" scale ($V \sim 125$ km s^{-1}), gas-dominated quasi-bulgeless Sd–Im galaxies become numerically dominant; while (2) above the "bimodality" scale ($V \sim 200$ km s^{-1}), gas-starved E/S0s become the norm. Notwithstanding these transitions, galaxy mass (or V as its proxy) is a poor predictor of gas-to-stellar mass ratio $M_{\rm gas}/M_*$. Instead, $M_{\rm gas}/M_*$ correlates well with the ratio of a galaxy's stellar mass formed in the last Gyr to its preexisting stellar mass, such that the two ratios have numerically similar values. This striking correspondence between *past*-averaged star formation and *current* gas richness implies routine refueling of star-forming galaxies on Gyr timescales. We argue that this refueling underlies the tight $M_{\rm gas}/M_*$ versus color correlations often used to measure "photometric gas fractions." Furthermore, the threshold and bimodality scale transitions reflect mass-dependent demographic shifts between three refueling regimes—*accretion-dominated, processing-dominated,* and *quenched*. In this picture, gas-dominated dwarfs are explained not by inefficient star formation but by overwhelming gas accretion, which fuels stellar mass doubling in $\lesssim$1 Gyr. Moreover, moderately gas-rich bulged disks such as the Milky Way are transitional, becoming abundant only in the narrow range between the threshold and bimodality scales.

Key word: galaxies: evolution

Online-only material: color figures, machine-readable table

1. INTRODUCTION

Galaxies grow both by merging and by fresh gas accretion. Hierarchical models that follow the merger histories of galaxies and their host dark matter halos successfully explain the large-scale structure of the universe, yet these models have difficulty reproducing the relative abundance of disk-dominated versus bulge-dominated galaxies across a broad range of environments (e.g., Navarro & White 1994; Abadi et al. 2003; D'Onghia & Burkert 2004; Stewart et al. 2008; Martig et al. 2009). Broadly speaking, this failure reflects the disk-destroying nature of stellar-mass-dominated mergers (and can therefore be mitigated by "quiet" merger histories such as may be found in low-density environments; Weinzirl et al. 2009; Fontanot et al. 2011).[13] On the other hand, gas-rich mergers are much less destructive and

may even help to build disks. Such mergers are expected to predominate at low galaxy masses and/or early epochs (e.g., Robertson et al. 2006; Hopkins et al. 2009; Stewart et al. 2009). Fresh gas accretion may also rebuild disks in low-mass E/S0 merger remnants, potentially restoring late-type morphologies (e.g., Cox et al. 2001; Morganti et al. 2006; Stark et al. 2013).

Observations point to significant cold gas accretion onto galaxies (Sancisi et al. 2008 and references therein). Moreover, the dynamics of halo gas suggest that this gas can in principle provide the angular momentum needed for the rapid growth of disks (Stewart et al. 2011). Cosmological hydro simulations show large-scale "cold" ($\sim10^5$–10^6 K) gas flows that travel along the filaments and walls of the cosmic web (e.g., Kereš et al. 2005). Observational signs of such flows have indeed been found (Zitrin & Brosch 2008; Stanonik et al. 2009; Narayanan et al. 2010; see also Giavalisco et al. 2011; Churchill et al. 2012). It is not yet clear to what extent these flows remain cold or shock-heat upon halo entry (compare Nelson et al. 2013 versus Birnboim & Dekel 2003 and Kereš et al. 2005). These details may affect angular momentum delivery as well as the onset of rapid accretion, which typically occurs when the cooling radius

---

[12] Adjunct Assistant Astronomer, National Radio Astronomy Observatory, P.O. Box 2, Green Bank, WV 24944, USA.

[13] The failure may also be compounded by the extreme loss of gas angular momentum in some simulations, although implementing star formation feedback and/or higher mass and force resolution can counteract this problem (e.g., Weil et al. 1998; Governato et al. 2007).

exceeds the virial radius, below a characteristic mass scale that depends on the model (Lu et al. 2011). Regardless of these specifics, it is a general feature of recent models that cosmic gas accretion accounts for a larger percentage of galaxy growth in low-mass halos than can be attributed to merging. Thus, the physics of accretion can dramatically change the balance of bulges and disks within the hierarchical merging paradigm.

Clearly mass-dependent gas physics affects patterns of growth by both mergers and accretion, and transitions in gas physics may lie at the heart of understanding the disky morphologies and overall growth histories of galaxies. Two galaxy mass scales have been previously noted as important transition points in morphology, gas richness (defined as gas-to-stellar mass ratio in this paper), and star formation history (SFH): the "bimodality scale" and the "gas-richness threshold scale."

The bimodality scale is typically identified with stellar mass $M_* \sim 10^{10.5} \, M_\odot$, which corresponds to rotation velocity $V \sim 200$ km s^{-1} (see Section 3 herein). This scale marks the crossover point in relative abundance of young disk-dominated versus old spheroid-dominated stellar populations (Kauffmann et al. 2003a). As traced by late-type versus early-type morphology, this transition appears to shift downward in mass over cosmic time (Bundy et al. 2005). Equivalently, the bimodality scale marks a shift in the relative number density of galaxies on the red and blue sequences in $u - r$ color versus stellar mass M_* parameter space (Baldry et al. 2004), which are associated with "red and dead" galaxies that have a strong 4000 Å break and blue star-forming systems, respectively. Active galactic nucleus (AGN) activity in early-type galaxies peaks up just below the bimodality scale in a population that may be evolving toward the red sequence, suggesting black hole growth in tandem with spheroid formation (Schawinski et al. 2010). The slope of the gas-phase metallicity versus M_* relation flattens above the bimodality scale, indicating changes in the interplay of gas cooling/infall, gas consumption, and gas loss in metal-enriched outflows (Tremonti et al. 2004). Hot gas halos become common above the bimodality scale (Mulchaey & Jeltema 2010, translating their K-band magnitudes to equivalent stellar masses), potentially enhancing the efficacy of AGN feedback (Dekel & Birnboim 2006).

A second, lower-mass transition scale was previously highlighted by Dekel & Silk (1986), in a scenario explaining low-metallicity diffuse dwarf galaxies as the result of global gas loss caused by supernova winds acting in the shallow potential wells of $V \lesssim 100$ km s^{-1} dark matter halos. More recent work has shown that such "blowaway" (as distinct from local "blowout") should occur only in much smaller halos, near $V \sim 30$ km s^{-1} (Mac Low & Ferrara 1999). Blowaway near $V \sim 100$ km s^{-1} would in any case be hard to reconcile with the fact that "high-mass dwarf" galaxies are typically gas-rich rather than gas-poor (e.g., Bettoni et al. 2003; Kannappan 2004, hereafter K04). In fact, gas-*dominated* galaxies become typical of the blue sequence below $M_* \sim 10^{9.5-10} \, M_\odot$ (corresponding to $V \sim 125$ km s^{-1}; Section 3 herein), as gas fractions rise on both sequences (K04[14]; Kannappan & Wei 2008; Kannappan et al. 2009, hereafter KGB). We therefore refer to the $V \sim 125$ km s^{-1} scale as the "gas-richness threshold scale," following KGB. Calculations by Dalcanton (2007) suggest that an increase in gas-richness is essential to explain changes in

metallicity at the threshold scale (specifically, the drop in effective yields below $V \sim 125$ km s^{-1} reported by Garnett 2002), and that a second essential ingredient is low star formation efficiency (in the sense of star formation rate divided by gas mass; we will revisit this concept in relation to cosmic accretion in Section 4.4.2).

In a separate study of edge-on, "bulgeless" disk galaxies, Dalcanton et al. (2004) reported another presumably related change in interstellar medium (ISM) physics at the threshold scale: thin concentrated dust lanes emerge abruptly above $V \sim 120$ km s^{-1}. Moreover, despite the authors' best efforts to select for bulgeless morphology, in practice their high-quality follow-up imaging reveals a small "three-dimensional" bulge in every sample galaxy above $V \sim 120$ km s^{-1}, suggesting a link between changes in gas physics and galaxy structure. The onset of inevitable bulges above the threshold scale (also seen by Bell 2008) occurs simultaneously with a sharp *decline* in the population of "blue-sequence E/S0s," identified by KGB as gas-rich merger remnants rebuilding disks (although higher-mass blue E/S0s are more often quenching, especially above the bimodality scale; Schawinski et al. 2009; KGB). Fisher & Drory (2011) report transitions in bulge demographics at both the threshold and bimodality scales, with bulgeless galaxies dominant below $M_* \sim 10^{9.5} \, M_\odot$, pseudobulges dominant between $10^{9.5}$ and $10^{10.5} \, M_\odot$, and classical bulges/elliptical galaxies dominant above $10^{10.5} \, M_\odot$. Interestingly, the E/S0 mass–radius relation bifurcates into two loci below the threshold scale (e.g., KGB; Misgeld & Hilker 2011).

Given the variety of physical processes and galaxy properties changing at the threshold and bimodality scales, these closely spaced mass scales have been conflated by multiple authors, including K04 and Dekel & Birnboim (2006), and the blurring of the two has been further exacerbated by systematic differences in stellar-mass zero points between investigators (see Kannappan & Gawiser 2007; Kannappan & Wei 2008). Yet appreciating the distinction between the threshold and bimodality scales is of key interest, since we will demonstrate herein that only in the narrow mass range between the threshold and bimodality scales do galaxies like our Milky Way—intermediate between gas-dominated bulgeless disks and gas-starved spheroids—become typical in the galaxy population. An exploration of the transitions occurring at the threshold and bimodality scales may therefore shed light on our Galaxy's past and future.

In what follows we employ multi-wavelength data from two complementary samples described in Section 2 to explore structural and gas-richness (M_{gas}/M_*) transitions across the threshold and bimodality scales in Section 3. We show that notwithstanding these notable transitions, there is far greater scatter in M_{gas}/M_* versus galaxy mass than has been previously appreciated. In contrast, we demonstrate in Section 4 that M_{gas}/M_* correlates in a surprisingly one-to-one fashion with a quantity we refer to as the long-term fractional stellar mass growth rate (FSMGR$_{LT}$), which considers star formation integrated over the last Gyr and is defined such that it can exceed one over the unit of time, unlike a specific star formation rate (SSFR). We argue that the FSMGR$_{LT}$–M_{gas}/M_* correlation, and not the Kennicutt–Schmidt Law, underlies the tight observed relation between M_{gas}/M_* and ultraviolet/blue minus near-infrared colors (hereafter, U–NIR colors) previously reported by K04. Moreover, we propose that coordinated changes in morphology and gas richness as a function of FSMGR$_{LT}$ can be usefully understood in terms of changes in cosmic accretion and internal

---

[14] Identifying this shift in gas richness with the threshold scale requires shifting the stellar-mass zero point from Bell et al. (2003) as used by K04 to coincide with that of Kauffmann et al. (2003a).
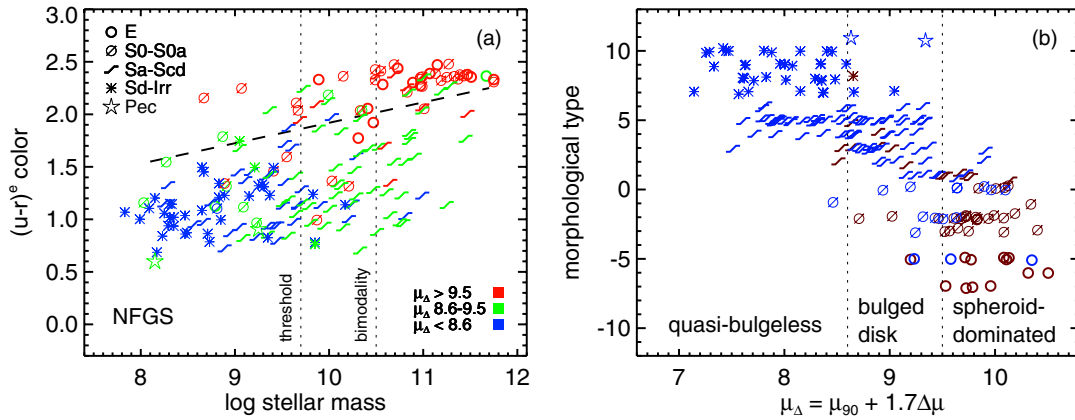
Figure 1. Morphological type, color, and stellar mass distribution of the Nearby Field Galaxy Survey (NFGS). (a) Distribution of NFGS galaxy morphologies in $(u - r)^e$ color vs. stellar mass M_* parameter space, with symbol color corresponding to the μ_Δ classes defined by the dividing lines in panel (b). Note that $(u - r)^e$ is a de-extincted color estimated by our stellar population modeling code and as such enhances the division between the red and blue sequences. However, it does not shift the basic locus of the red sequence significantly; rather, the bluer color of this locus compared to previous studies (e.g., Baldry et al. 2004) reflects improvements in our photometry compared to the SDSS pipeline, as described in Section 2.1.1 and Figure 2. (b) Calibration of the μ_Δ parameter used to distinguish quasi-bulgeless, bulged-disk, and spheroid-dominated galaxies (see Section 2.1.1). Symbol color corresponds to the red-/blue-sequence division shown in panel (a). Small random offsets have been applied to the morphological types to separate points.

(A color version of this figure is available in the online journal.)

gas processing between three "refueling regimes": accretion-dominated, processing-dominated, and quenched. Finally, we tie our results back to the threshold and bimodality scales, showing that these scales represent transitions in the relative numerical dominance of galaxies in the three regimes, likely tied to the halo mass dependence of cosmic accretion. Our results suggest a reevaluation of dwarf galaxies as not "inefficient" gas consumers but "overwhelmed" gas accretors, and of moderately gas-rich bulged disks like our Milky Way as not "normal" but "transitional" in the galaxy population.

2. DATA AND METHODS

Our analysis relies on two samples. The highest-quality H I data, multi-band photometry, and kinematic data come from the Nearby Field Galaxy Survey (NFGS; Jansen et al. 2000a, 2000b; Kannappan & Fabricant 2001; Kannappan et al. 2002; Wei et al. 2010a), a broadly representative sample of ~200 galaxies spanning stellar masses $M_* \sim 10^8$–$10^{12}\ M_\odot$ and all morphologies. Better statistics are offered by a volume-limited sample of ~3000 galaxies, hereafter the V3000 sample, with flux-limited H I data and partial kinematic information from the blind 21 cm Arecibo Legacy Fast ALFA (ALFALFA; Giovanelli et al. 2005; Haynes et al. 2011) survey, which we combine with reprocessed photometry from the Sloan Digital Sky Survey (SDSS; Aihara et al. 2011) Data Release 8 (DR8), the *GALEX* mission archive (Morrissey et al. 2007), and the Two Micron All Sky Survey (2MASS; Jarrett et al. 2000). We detail new and reprocessed archival data for the NFGS and V3000 samples below.

We assume $H_0 = 70$ km s^{-1} Mpc^{-1} and $d = cz/H_0$ throughout this work. Neglecting Λ introduces negligible errors at the low redshifts of our sample galaxies.

2.1. The Nearby Field Galaxy Survey

The NFGS was drawn from a *B*-selected parent survey, the CfA 1 Redshift Survey (Huchra et al. 1983), in approximate proportion to the luminosity function, and it preserves the CfA 1 survey's relative frequency of morphological types at each luminosity (Jansen et al. 2000b). The 196 galaxies in the NFGS obey an artificial luminosity–distance correlation imposed to

ensure that their apparent diameters do not vary too much, as an observational convenience. Thus, large-scale environments are not uniformly sampled as a function of luminosity, although a wide variety of environments are represented, ranging from underdense regions to the Coma Cluster. Our analysis makes use of 190/196 galaxies in the NFGS, after rejection of 6 objects with nearly point-source morphology due to powerful AGNs or in one case a superposed star.

Figure 1 illustrates the color, stellar mass, and morphology distribution of these 190 galaxies. We note that the Hubble type classifications in Figure 1(a) are reliable but not perfect, due to the inclination-blind selection of the NFGS as well as the fact that when the galaxies were classified, Jansen et al. (2000b) allowed fairly large discrepancies between different classifiers to remain unresolved. Following Kannappan et al. (2009), we reclassify the polar ring galaxy UGC 9562 as an S0. We also reclassify the very round dust-lane galaxy NGC 3499 as an E. Figure 1(b) defines a new quantitative morphology metric used as a complementary diagnostic, discussed in Section 2.1.1 below.

2.1.1. Photometry and Stellar Masses

Our analysis combines *UBR* photometry from Jansen et al. (2000b) and global (integrated slit-scanned) spectrophotometry from Jansen et al. (2000a) with our own custom reprocessed *GALEX* near-UV (NUV), SDSS *ugriz*, 2MASS *JHK*, and *Spitzer* IRAC 3.6 μm photometry, provided in Table 1. For the new photometric measurements we redetermine the position angle (P.A.) and axial ratio (b/a = ratio of semi-minor to semi-major axis) without reference to the Jansen et al. values, but our kinematic observations and analysis predate the new photometry and thus make use of measurements from Jansen et al. as detailed in Section 2.1.3 and Table 2. We adopt foreground Milky Way extinction corrections from Schlegel et al. (1998), except at 3.6 μm where such corrections are negligible, and we adjust the Jansen et al. photometry and spectrophotometry to match.

Initially, each galaxy is run through an optical photometric pipeline that produces masks and freely determines elliptical apertures from a deep *gri* coadded image (K. D. Eckert et al., in preparation). The outer disk P.A. and axial ratio are then fixed

Table 1
Photometry and Stellar Mass Estimates Table Description

Column	Description
1	NFGS ID number
2	Object name
3	*GALEX* NUV magnitude[a,b]
4	Error on *GALEX* NUV magnitude
5	SDSS *u* magnitude[a]
6	Error on SDSS *u* magnitude
7	SDSS *g* magnitude[a]
8	Error on SDSS *g* magnitude
9	SDSS *r* magnitude[a]
10	Error on SDSS *r* magnitude
11	SDSS *i* magnitude[a]
12	Error on SDSS *i* magnitude
13	SDSS *z* magnitude[a]
14	Error on SDSS *z* magnitude
15	2MASS *J* magnitude[a]
16	Error on 2MASS *J* magnitude
17	2MASS *H* magnitude[a]
18	Error on 2MASS *H* magnitude
19	2MASS *K* magnitude[a]
20	Error on 2MASS *K* magnitude
21	*Spitzer* IRAC 3.6μm magnitude
22	Error on *Spitzer* IRAC 3.6μm magnitude
23	Log of stellar mass
24	Log of stellar mass from KGB[c]
25	SDSS *r*-band 50% light radius
26	SDSS *r*-band 90% light radius

Notes.

[a] NUV*ugrizJHK* magnitudes are reported with foreground extinction corrections determined from the Schlegel et al. (1998) dust maps using the extinction curves of O'Donnell (1994) and Cardelli et al. (1989) in the optical and UV, respectively.

[b] We assume an effective wavelength of 2271 Å for the *GALEX* NUV filter.

[c] Stellar masses derived by Kannappan et al. (2009) (not used in this paper).

(This table is available in its entirety in a machine-readable form in the online journal. A portion is shown here for guidance regarding its form and content.)

and used to determine a second set of elliptical apertures imposed on all bands NUV+*ugrizJHK*+IRAC 3.6 μm, enabling robust extrapolation of total magnitudes, even at low signal-to-noise ratio (S/N). Final magnitudes and systematic errors are calculated from a comparison of different methods (exponential profile fitting, curve-of-growth, outer-disk color correction, and large-aperture magnitude) for each band. Our SDSS magnitudes are measured using the newly optimized background sky estimates provided with all DR8 images (though not actually incorporated in DR8 catalog photometry), as described in Blanton et al. (2011). The extended sky coverage of DR8 includes 177 of our 190 galaxies. For *GALEX* we adopt the background estimation provided by the mission pipeline (Morrissey et al. 2007), and the available coverage yields NUV magnitudes for 93 of the 190 galaxies.

In the near-IR, custom background subtraction is necessary. IRAC 3.6 μm images are available for 107 of our sample galaxies, mainly courtesy of the Spitzer Survey of Stellar Structure in Galaxies (S4G; Sheth et al. 2010) and our own program targeting low-mass E/S0 galaxies (GO-30406, PI: Kannappan). We calculate 3.6 μm magnitudes using the level 2 (PBCD) images produced by the *Spitzer* pipeline, which have a residual

low-level, non-uniform background. To remove this, we mask the primary galaxy and any other bright objects in each frame, and the remaining image is convolved with a median filter of size roughly four times the optical size of the galaxy to create a smooth background map. This map is subtracted from the original image to yield the image on which we perform photometric measurements. The resulting magnitudes are in good agreement with those from Moffett et al. (2012), who applied a similar background subtraction technique, with typical differences of ~0.04 mag. In turn, our 2MASS pipeline incorporates background subtraction methods optimized with reference to the IRAC imaging, which includes deep S4G imaging of dwarf galaxies. With this careful background subtraction and the imposition of ellipses determined from the optical profile fits (using the P.A.s and ellipticities from Jansen et al. 2000b for the 13 galaxies lacking SDSS data), we have found it possible to compute reliable *JHK* magnitudes for the entire sample, albeit sometimes with large error bars. As in the optical, we use multiple extrapolation techniques to estimate systematic errors in the NIR, although we find that a curve-of-growth approach is generally most robust, especially for shallow 2MASS data (see Stark et al. 2013, hereafter S13, for further details on our NIR pipelines). It is noteworthy that our 2MASS magnitudes are well behaved in combined stellar population fits of optical and NIR data that include high-quality spectrophotometry and deep IRAC photometry.

Table 1 lists our NUV+*ugrizJHK*+3.6 μm magnitudes (including foreground Milky Way extinction corrections), with uncertainties determined by combining Poisson errors with systematic errors from profile extrapolation. The IRAC magnitude errors include an extra 10% uncertainty associated with the "aperture corrections" required for profiles extrapolated to infinity, which we have applied as prescribed by the *Spitzer* IRAC instrument handbook.[15]

As illustrated in Figure 2, our $u - r$ colors are systematically ~0.2 mag bluer than those determined from SDSS catalog photometry, which is also evident in the fact that the red sequence in Figure 1 is ~0.2 mag bluer than in previous studies using SDSS catalog data. However, the same figure shows that our colors are in close agreement with those determined by Jansen et al. (2000b). We attribute about half of the offset between our $u - r$ colors and those from the SDSS catalog to the improved sky subtraction of Blanton et al. (2011), who demonstrate that their new protocol will yield ~0.1 mag bluer colors for galaxies with $\log r_{50} \gtrsim 1.4$ (marked in Figure 2). However, we measure greater color differences than expected from the new sky subtraction alone. Some discrepancies certainly reflect catastrophic failures of the SDSS pipeline (a few so extreme they lie outside the plot boundaries), but some likely also reflect the fact that we (like Jansen et al. 2000b) measure magnitudes by methods that permit color gradients, whereas the SDSS model magnitude algorithm enforces a common profile in all bands, which is determined in the r band.[16] In the case of massive early-type galaxies, for which the centers are redder than the outskirts (e.g., La Barbera et al. 2010), the SDSS model magnitude methodology would be expected to produce an "overly red" red sequence.

Stellar masses and other stellar population parameters are estimated using a variant of the code described in Kannappan & Gawiser (2007) and improved by KGB, which simultaneously

---

[15] http://irsa.ipac.caltech.edu/data/SPITZER/docs/irac/iracinstrumenthandbook/

[16] http://www.sdss.org/dr7/algorithms/photometry.html#mag_model

Table 2
Kinematic and H I Data for the NFGS

ID	P.A.[a] (°)	i [b] (°)	V_{pmm} [c] (km s^{-1})	r_e [d] ('')	Extent ('')	Asym. (%)	W_{50} [e] (km s^{-1})	$\sigma_{r_e/4}$ (km s^{-1})	V_* [f] (km s^{-1})	V [g] (km s^{-1})	log M_{HI} [h] (log $M_\odot$)	H I Range[j] (km s^{-1})
1	160/160	39.9	⋯	7.1	⋯	⋯	⋯	133 ± 10	120	188 ± 14^{sd}	<8.32	4661–4904
2	10/10	56.9	52	12.1	13.6	4.8	[W10a]	22 ± 8^l	66	99 ± 19^{sr}	W10a‡	⋯
3	55/48	20.2	⋯	28.8	⋯	⋯	W10a	188 ± 11	⋯	266 ± 16^{sd}	W10a	⋯
4	168/160	0.0	58	11.7	22.7	2.9	W10a	61 ± 8^l	⋯	$[87 \pm 12]^{sd}$	W10a	⋯
5	24/25	78.0	217	32.1	47.6	5.3	W10a	106 ± 10^l	⋯	221 ± 11^{ir}	W10a	⋯
7	-/48	34.3	⋯	32.3	⋯	⋯	W10a	316 ± 18	⋯	447 ± 25^{sd}	W10a	⋯
8	24/25	62.1	173	10.6	22.7	1.3	W10a	132 ± 10^l	171	215 ± 28^{sr}	W10a	⋯
10	110*/110*	0.0	⋯	6.6	⋯	⋯	⋯	174 ± 11	17	247 ± 16^{sd}	<9.02^k	5094–5339
11	-/90	27.9	⋯	4.5	⋯	⋯	$[54 \pm 40]$	115 ± 9	28	163 ± 13^{sd}	$8.62 \pm 0.20^\dagger$	5322–5471
12	90/90	51.4	154	9.5	12.5	1.1	$[318 \pm 42]$	121 ± 12^l	163	232 ± 31^{sr}	$9.67 \pm 0.10^\dagger$	9650–10716
13	122.5/-	0.0	[37]	23.2	23.8	9.0	[W10a]	⋯	⋯	⋯	W10a‡	⋯
14	-/44	74.2	⋯	17.3	⋯	⋯	⋯	49 ± 8^l	76	97 ± 17^{sr}	<7.57	2355–2548
15	2.5/5	49.5	9	13.1	15.9	9.4	W10a	28 ± 11^l	⋯	68 ± 10^{nr}	W10a	⋯
16	90*/90*	27.9	93	8.2	19.3	2.3	W10a	79 ± 12^l	⋯	$[289 \pm 146]^{nr}$	W10a	⋯
17	168/-	39.9	87	6.0	20.4	5.8	W10a	⋯	⋯	$[150 \pm 44]^{ir}$	W10a	⋯
18	30/-	37.8	[11]	61.7	29.5	37.0	W10a	⋯	⋯	$[44 \pm 10]^{ir}$	W10a	⋯
19	40/44	26.4	75	7.6	14.7	2.9	W10a	⋯	⋯	$[358 \pm 172]^{nr}$	W10a	⋯
21	132.5/-	62.1	61	45.2	69.2	4.9	W10a	⋯	⋯	83 ± 10^{ir}	W10a	⋯
22	-/135	59.7	⋯	10.7	⋯	⋯	$[374 \pm 10]$	134 ± 10	⋯	190 ± 14^{sd}	$9.69 \pm 0.02^\dagger$	3526–3829
23	54/55	62.1	164	12.9	28.3	3.8	[W10a]	87 ± 8^l	⋯	189 ± 22^{ir}	W10a‡	⋯
24	132.5*/-	17.3	39	22.2	36.3	12.1	W10a	⋯	⋯	$[187 \pm 61]^{nr}$	W10a	⋯
25	43/43	62.1	128	16.6	27.2	0.9	W10a	60 ± 8^l	⋯	163 ± 19^{nr}	W10a	⋯
26	54/-	66.4	223	15.5	62.4	2.7	W10a	⋯	⋯	249 ± 15^{nr}	W10a	⋯
27	70*/-	0.0	49	16.3	31.8	8.3	W10a	⋯	⋯	⋯	W10a	⋯
28	12/-	71.1	50	29.4	30.6	4.9	W10a	⋯	⋯	67 ± 10^{ir}	W10a	⋯
29	120/-	49.5	[197]	22.6	17.0	1.9	W10a	⋯	⋯	377 ± 31^{nr}	W10a	⋯
30	70/70	75.8	⋯	13.7	⋯	⋯	$[261 \pm 8]$	186 ± 12	205	262 ± 17^{sd}	$9.88 \pm 0.01^\dagger$	3428–3850
32	45*/-	39.9	41	46.1	61.2	3.5	W10a	⋯	⋯	$[84 \pm 11]^{ir}$	W10a	⋯
33	-/70	24.1	⋯	11.4	⋯	⋯	$[84 \pm 3]$	177 ± 14	⋯	250 ± 19^{sd}	9.15 ± 0.10	6367–6529
34	90*/90*	0.0	113	8.9	19.3	2.3	$[203 \pm 6]$	122 ± 11^l	79	$[172 \pm 15]^{sd}$	$10.24 \pm 0.03^\dagger$	8100–8418
35	110/110	42.5	⋯	22.6	⋯	⋯	$[277 \pm 15]$	241 ± 15	⋯	341 ± 21^{sd}	9.10 ± 0.06	4598–4957
36	165/170	78.0	⋯	19.8	⋯	⋯	W10a	170 ± 11^l	⋯	240 ± 15^{sd}	W10a	⋯
37	1/170	48.1	259	21.5	35.2	1.9	W10a	234 ± 14^l	⋯	348 ± 35^{nr}	W10a	⋯
38	1/-	85.0	54	33.7	52.2	3.0	[W10a]	⋯	⋯	67 ± 10^{ir}	W10a‡	⋯
39	150/151	46.8	123	15.2	22.7	4.0	W10a	47 ± 19^l	99	194 ± 39^{nr}	W10a	⋯
40	80/90	54.7	⋯	40.9	⋯	⋯	⋯	⋯	⋯	⋯	<6.58	522–675
41	130/-	82.4	53	25.2	31.8	6.9	[W10a]	⋯	⋯	66 ± 10^{ir}	W10a‡	⋯
42	-/170	54.7	⋯	45.6	⋯	⋯	$[146 \pm 86]$	122 ± 9	⋯	172 ± 13^{sd}	8.44 ± 0.19	2570–2930
43	13/14	64.0	148	18.4	43.1	2.6	W10a	110 ± 9^l	⋯	174 ± 11^{nr}	W10a	⋯
44	52/50	27.9	59	6.7	18.1	5.4	159 ± 4	54 ± 7^l	24	$[170 \pm 86]^{nr}$	8.53 ± 0.03	1420–1665
45	115*/-	29.6	3	12.4	18.1	14.4	W10a	⋯	⋯	$[415 \pm 221]^{nr}$	W10a	⋯
46	1*/-	31.7	77	10.9	19.3	5.6	[W10a]	⋯	⋯	$[167 \pm 94]^{ir}$	W10a‡	⋯
47	76/-	57.3	[68]	37.2	28.3	6.1	W10a	⋯	⋯	102 ± 7^{nr}	W10a	⋯
48	130/-	49.5	136	21.4	37.4	3.8	W10a	⋯	⋯	186 ± 28^{ir}	W10a	⋯
49	103/100	66.1	127	13.8	29.5	0.6	W10a	66 ± 15^l	⋯	146 ± 12^{ir}	W10a	⋯
50	40/-	51.7	59	46.8	60.1	10.2	W10a	⋯	⋯	91 ± 11^{ir}	W10a	⋯
51	103/-	62.1	61	25.1	31.8	1.6	W10a	⋯	⋯	82 ± 11^{ir}	W10a	⋯
52	1/-	62.1	53	20.8	28.3	6.1	[W10a]	⋯	⋯	73 ± 11^{ir}	W10a‡	⋯
53	144/-	54.7	78	36.8	64.6	5.8	W10a	⋯	⋯	123 ± 6^{nr}	W10a	⋯
54	-/50	81.2	⋯	13.6	⋯	⋯	⋯	195 ± 11	218	276 ± 16^{sd}	<8.97	6913–7433
55	101/-	37.8	27	15.2	22.7	6.1	[W10a]	⋯	⋯	$[68 \pm 21]^{ir}$	W10a‡	⋯
56	130/140	44.5	64	18.7	29.5	3.1	W10a	36 ± 10^l	⋯	109 ± 21^{nr}	W10a	⋯
57	1/-	67.2	55	41.7	76.0	9.4	W10a	⋯	⋯	74 ± 3^{nr}	W10a	⋯
58	154/-	90.0	170	43.3	45.4	1.5	W10a	⋯	⋯	173 ± 10^{ir}	W10a	⋯
59	110/110	27.9	41	6.5	7.9	2.7	104 ± 27	38 ± 10^l	73	$[193 \pm 99]^{sr}$	8.60 ± 0.05	3100–3600
60	1/-	85.5	145	24.4	31.8	1.6	W10a	⋯	⋯	151 ± 7^{nr}	W10a	⋯
61	114/-	59.7	169	15.3	30.6	2.4	W10a	⋯	⋯	200 ± 18^{ir}	W10a	⋯
62	54/-	75.8	68	19.4	31.8	6.5	W10a	⋯	⋯	82 ± 10^{ir}	W10a	⋯
63	40/-	84.6	71	18.1	31.8	5.5	W10a	⋯	⋯	82 ± 10^{ir}	W10a	⋯
64	40/-	31.7	40	7.4	10.2	6.4	W10a	⋯	⋯	$[210 \pm 118]^{nr}$	W10a	⋯
65	121/120	84.8	333	23.6	36.3	1.4	708 ± 7	231 ± 14^l	306	355 ± 4^{nr}	10.16 ± 0.03	10367–11208
66	130/140	0.0	95	9.1	23.8	2.6	W10a	78 ± 8^l	⋯	$[110 \pm 12]^{sd}$	W10a	⋯
67	144/140	26.4	136	15.4	26.1	7.1	279 ± 3	124 ± 10^l	⋯	$[319 \pm 154]^{ir}$	9.90 ± 0.04	7920–8242

Table 2
(Continued)

ID	P.A.[a] (°)	i[b] (°)	$V_{\rm pmm}$[c] (km s^{-1})	r_e[d] (″)	Extent (″)	Asym. (%)	W_{50}[e] (km s^{-1})	$\sigma_{r_{e/4}}$ (km s^{-1})	V_*[f] (km s^{-1})	V[g] (km s^{-1})	log $M_{\rm HI}$[h] (log $M_\odot$)	H I Range[j] (km s^{-1})
68	172/170	66.1	67	14.5	19.3	8.1	140 ± 7	$\cdots$	$\cdots$	85 ± 13^{ir}	7.89 ± 0.02	535–869
69	100*/100*	0.0	8	4.0	5.7	19.3	136 ± 10	$46 \pm 11^{\,l}$	21	$[64 \pm 16]^{sd}$	9.64 ± 0.02	5644–6023
70	116/-	86.6	102	31.3	45.4	2.0	W10a	$\cdots$	$\cdots$	111 ± 10^{ir}	W10a	$\cdots$
71	54/-	79.6	111	23.0	39.7	4.5	W10a	$\cdots$	$\cdots$	123 ± 4^{nr}	W10a	$\cdots$
72	-/50*	90(29.6)	$\cdots$	7.6	$\cdots$	$\cdots$	$[257 \pm 11]$	$61 \pm 7^{\,l}$	49	$[133 \pm 74]^{sr}$	8.07 ± 0.06	1358–1725
73	165/-	85.5	86	42.9	88.5	6.4	W10a	$\cdots$	$\cdots$	96 ± 10^{ir}	W10a	$\cdots$
75	-/122	56.0	$\cdots$	14.8	$\cdots$	$\cdots$	$[245 \pm 60]$	99 ± 8	$\cdots$	141 ± 12^{sd}	8.62 ± 0.05	934–1489
76	90/-	63.6	107	43.8	62.4	4.6	W10a	$\cdots$	$\cdots$	128 ± 11^{ir}	W10a	$\cdots$
77	165/170	69.3	163	27.0	65.8	1.0	[W10a]	$74 \pm 12^{\,l}$	$\cdots$	178 ± 12^{ir}	W10a‡	$\cdots$
78	-/100	45.6	$\cdots$	8.1	$\cdots$	$\cdots$	$\cdots$	195 ± 13	$\cdots$	276 ± 18^{sd}	<8.87	7368–7750
79	20/-	43.0(58.1)	113	8.4	15.9	5.2	$[263 \pm 16]$	$\cdots$	$\cdots$	177 ± 31^{ir}	$10.67 \pm 0.01^\dagger$	12500–13076
80	-/18	62.1	$\cdots$	20.6	$\cdots$	$\cdots$	$\cdots$	88 ± 7	$\cdots$	124 ± 10^{sd}	<6.62	549–772
81	165/170	76.2	90	24.3	29.5	2.5	W10a	$69 \pm 21^{\,l}$	$\cdots$	103 ± 11^{ir}	W10a	$\cdots$
82	76/-	74.2	[151]	23.1	20.4	3.9	[W10a]	$\cdots$	$\cdots$	$[161 \pm 12]^{ir}$	W10a‡	$\cdots$
83	125/125	42.5	11	6.0	7.9	21.6	[W10a]	$\cdots$	23	59 ± 25^{sr}	W10a‡	$\cdots$
84	11/-	52.1	51	64.6	72.6	4.1	W10a	$\cdots$	$\cdots$	83 ± 4^{nr}	W10a	$\cdots$
85	133/140	75.4	131	19.3	26.1	3.2	W10a	$56 \pm 11^{\,l}$	$\cdots$	142 ± 11^{ir}	W10a	$\cdots$
86	-/170	51.4	$\cdots$	19.9	$\cdots$	$\cdots$	$\cdots$	257 ± 15	$\cdots$	363 ± 21^{sd}	<9.07	9245–9786
87	122/122	62.1	[23]	9.5	7.9	2.4	100 ± 6	$49 \pm 9^{\,l}$	$\cdots$	$[70 \pm 13]^{sd}$	8.65 ± 0.02	1489–1794
88	172/-	90.0	94	32.0	56.7	2.8	W10a	$\cdots$	$\cdots$	105 ± 4^{nr}	W10a	$\cdots$
89	80/-	37.8	46	37.9	54.4	11.2	W10a	$\cdots$	$\cdots$	$[95 \pm 13]^{ir}$	W10a	$\cdots$
90	54/-	29.6	115	9.2	22.7	4.0	171 ± 5	$\cdots$	$\cdots$	$[248 \pm 132]^{ir}$	10.64 ± 0.01	10660–11110
91	52/50	80.2	106	25.6	53.3	1.9	W10a	$\cdots$	$\cdots$	116 ± 10^{ir}	W10a	$\cdots$
92	73/73	66.1	48	7.6	11.3	0.9	[W10a]	$40 \pm 14^{\,l}$	34	67 ± 12^{ir}	W10a‡	$\cdots$
93	18/18	54.7	[4]	7.6	9.1	19.5	51 ± 3	$\cdots$	$\cdots$	$[31 \pm 8]^{nr}$	7.44 ± 0.02	682–824
94	40/-	31.7	60	23.1	44.2	4.8	W10a	$\cdots$	$\cdots$	$[143 \pm 24]^{nr}$	W10a	$\cdots$
95	131/-	65.4	82	36.3	45.4	7.7	[W10a]	$\cdots$	$\cdots$	102 ± 11^{ir}	W10a‡	$\cdots$
96	100/100	45.6	[24]	5.6	5.7	20.7	102 ± 10	$34 \pm 12^{\,l}$	14	$[71 \pm 21]^{nr}$	7.83 ± 0.05	992–1252
97	165/-	21.5	[23]	40.7	39.7	7.7	W10a	$\cdots$	$\cdots$	$[102 \pm 22]^{ir}$	W10a	$\cdots$
98	170/170	79.4	[93]	15.5	11.3	3.0	W10a	$\cdots$	$\cdots$	136 ± 6^{nr}	W10a	$\cdots$
99	146/-	29.0	82	39.5	61.2	3.1	W10a	$\cdots$	$\cdots$	$[189 \pm 31]^{ir}$	W10a	$\cdots$
100	90.5/100	20.2	96	16.4	36.3	3.1	W10a	$174 \pm 15^{\,l}$	$\cdots$	$[304 \pm 114]^{ir}$	W10a	$\cdots$
101	40*/-	17.5	53	48.5	79.4	9.8	W10a	$\cdots$	$\cdots$	$[217 \pm 36]^{ir}$	W10a	$\cdots$
102	80/-	51.1	67	21.3	36.3	2.6	[W10a]	$\cdots$	$\cdots$	100 ± 14^{ir}	W10a‡	$\cdots$
103	1/6	44.9	91	25.2	37.4	3.5	[W10a]	$\cdots$	$\cdots$	142 ± 19^{ir}	W10a‡	$\cdots$
104	172/-	77.3	81	25.2	44.2	3.9	W10a	$\cdots$	$\cdots$	94 ± 10^{ir}	W10a	$\cdots$
105	100/100	62.1	11	8.4	10.2	6.7	73 ± 4	$38 \pm 14^{\,l}$	31	54 ± 18^{sr}	8.81 ± 0.01	1389–1663
106	18/18	72.2	[46]	16.8	7.9	3.2	$[253 \pm 39]$	$66 \pm 8^{\,l}$	$\cdots$	$[94 \pm 11]^{sd}$	$8.51 \pm 0.04^\dagger$	873–1150
107	165/-	84.3	100	30.4	45.4	3.4	W10a	$\cdots$	$\cdots$	109 ± 10^{ir}	W10a	$\cdots$
108	80/-	53.6	[49]	16.9	13.6	3.6	[W10a]	$\cdots$	$\cdots$	$[77 \pm 13]^{ir}$	W10a‡	$\cdots$
109	80/-	51.4	72	18.2	35.2	3.2	W10a	$\cdots$	$\cdots$	106 ± 16^{ir}	W10a	$\cdots$
110	40/-	69.3	75	18.4	34.0	7.6	W10a	$\cdots$	$\cdots$	93 ± 8^{nr}	W10a	$\cdots$
111	146/-	0.0	19	61.5	70.3	9.3	W10a	$\cdots$	$\cdots$	$\cdots$	W10a	$\cdots$
112	40/-	81.2	118	26.9	44.2	2.8	W10a	$\cdots$	$\cdots$	126 ± 10^{ir}	W10a	$\cdots$
113	108/110	68.8	[25]	40.7	37.4	6.1	W10a	$\cdots$	$\cdots$	$[43 \pm 10]^{ir}$	W10a	$\cdots$
114	40/-	77.3	146	26.3	46.5	1.9	W10a	$\cdots$	$\cdots$	154 ± 11^{ir}	W10a	$\cdots$
115	-/110*	26.4	$\cdots$	15.6	$\cdots$	$\cdots$	$[227 \pm 14]$	248 ± 15	$\cdots$	351 ± 21^{sd}	$10.11 \pm 0.02^\dagger$	8312–8634
116	131/-	54.7	65	32.3	64.6	8.0	W10a	$\cdots$	$\cdots$	106 ± 6^{nr}	W10a	$\cdots$
117	-/46*	29.6	$\cdots$	8.4	$\cdots$	$\cdots$	$\cdots$	59 ± 7	24	83 ± 10^{sd}	<6.02	607–703
118	1*/-	23.1	10	25.0	30.6	15.4	W10a	$\cdots$	$\cdots$	$[86 \pm 37]^{nr}$	W10a	$\cdots$
120	63/-	29.6	[20]	59.1	47.6	3.9	W10a	$\cdots$	$\cdots$	$[70 \pm 12]^{ir}$	W10a	$\cdots$
121	89/-	52.8	24	15.9	29.5	21.2	W10a	$\cdots$	$\cdots$	48 ± 11^{ir}	W10a	$\cdots$
122	18/-	39.4	31	24.3	39.7	3.1	[W10a]	$\cdots$	$\cdots$	$[71 \pm 13]^{ir}$	W10a‡	$\cdots$
123	40/-	78.9	105	51.6	93.0	5.1	W10a	$\cdots$	$\cdots$	115 ± 10^{ir}	W10a	$\cdots$
124	33/-	54.7	28	10.5	21.5	30.2	[W10a]	$\cdots$	$\cdots$	52 ± 12^{ir}	W10a‡	$\cdots$
125	100/100	45.6	99	11.7	21.5	6.0	242 ± 4	$61 \pm 13^{\,l}$	$\cdots$	169 ± 49^{nr}	9.97 ± 0.02	6680–7124
126	80/-	44.9	27	30.1	35.2	25.6	W10a	$\cdots$	$\cdots$	59 ± 12^{ir}	W10a	$\cdots$
127	159/-	79.6	[86]	47.6	57.8	6.9	W10a	$\cdots$	$\cdots$	$[97 \pm 10]^{ir}$	W10a	$\cdots$
128	115/116	31.7	34	22.9	10.2	28.7	[W10a]	$160 \pm 10^{\,l}$	178	$[374 \pm 64]^{sr}$	W10a‡	$\cdots$
129	-/30*	42.5	$\cdots$	8.2	$\cdots$	$\cdots$	$\cdots$	203 ± 12	$\cdots$	286 ± 17^{sd}	<8.83	6801–7176
130	-/135*	0.0	$\cdots$	8.0	$\cdots$	$\cdots$	$\cdots$	172 ± 11	$\cdots$	243 ± 15^{sd}	$<9.67^{k}$	6170–6408
131	-/71*	25.2	$\cdots$	13.1	$\cdots$	$\cdots$	$\cdots$	266 ± 15	$\cdots$	376 ± 22^{sd}	<8.77	7710–8075
132	100/100	47.8	105	17.1	36.3	2.7	W10a	$49 \pm 12^{\,l}$	$\cdots$	152 ± 20^{ir}	W10a	$\cdots$

Table 2
(Continued)

ID	P.A.[a] (°)	i[b] (°)	V_{pmm}[c] (km s^{-1})	r_e[d] (″)	Extent (″)	Asym. (%)	W_{50}[e] (km s^{-1})	$\sigma_{r_e/4}$ (km s^{-1})	V_*[f] (km s^{-1})	V[g] (km s^{-1})	log $M_{\rm H\,I}$[h] (log $M_\odot$)	H I Range[j] (km s^{-1})
133	80/-	75.8	85	23.3	35.2	5.7	208 ± 2	$\cdots$	$\cdots$	107 ± 4^{nr}	9.79 ± 0.01	2340–2760
134	172/-	90.0	88	35.7	57.8	4.8	W10a	$\cdots$	$\cdots$	98 ± 10^{ir}	W10a	$\cdots$
135	40/-	29.6	65	11.1	19.3	7.4	156 ± 2	$\cdots$	$\cdots$	$[158 \pm 84]^{nr}$	9.39 ± 0.02	3179–3596
136	153/-	65.4	101	27.4	53.3	4.9	W10a	$\cdots$	$\cdots$	121 ± 11^{ir}	W10a	$\cdots$
137	100*/100*	39.7	[82]	9.4	6.8	$\cdots$	W10a	101 ± 8	$\cdots$	143 ± 12^{sd}	W10a	$\cdots$
138	1/170*	75.1	285	26.3	55.6	4.9	W10a	196 ± 12^{l}	$\cdots$	309 ± 24^{nr}	W10a	$\cdots$
139	-/170	71.1	$\cdots$	18.0	$\cdots$	$\cdots$	$[402 \pm 10]$	257 ± 15	$\cdots$	363 ± 22^{sd}	$9.50 \pm 0.05^{\ddagger k}$	$\cdots$
140	1*/-	31.7	23	28.1	46.5	9.9	W10a	$\cdots$	$\cdots$	$[141 \pm 23]^{nr}$	W10a	$\cdots$
141	100/-	77.3	69	27.4	31.8	4.0	W10a	$\cdots$	$\cdots$	95 ± 5^{nr}	W10a	$\cdots$
142	60/56	72.4	290	21.7	32.9	1.4	W10a	175 ± 12^{l}	249	298 ± 17^{ir}	W10a	$\cdots$
143	168/-	76.2	114	20.3	30.6	3.2	W10a	$\cdots$	$\cdots$	125 ± 11^{ir}	W10a	$\cdots$
144	100/100	57.3	[21]	22.9	4.5	11.5	$46 \pm 16^{\dagger\dagger}$	45 ± 11^{l}	$\cdots$	$[64 \pm 16]^{sd}$	7.50 ± 0.06	668–925
145	18/16	79.6	[139]	52.9	62.4	3.5	W10a	34 ± 9^{l}	$\cdots$	$[146 \pm 10]^{ir}$	W10a	$\cdots$
146	-/30	78.7	$\cdots$	10.9	$\cdots$	$\cdots$	$\cdots$	142 ± 10	153	201 ± 14^{sd}	<7.94	1900–2282
147	-/100	45.6	$\cdots$	19.1	$\cdots$	$\cdots$	$\cdots$	194 ± 12	$\cdots$	275 ± 16^{sd}	<8.50	5230–5610
148	127/-	82.6	109	28.1	48.8	1.4	W10a	$\cdots$	$\cdots$	118 ± 10^{ir}	W10a	$\cdots$
149	40/36	83.3	$\cdots$	14.7	$\cdots$	$\cdots$	$\cdots$	151 ± 10	164	213 ± 14^{sd}	<8.39	3632–4040
150	65/56	90.0	[120]	46.2	59.0	2.1	W10a	30 ± 15^{l}	$\cdots$	$[127 \pm 10]^{ir}$	W10a	$\cdots$
151	80/-	52.8	227	17.1	44.2	1.9	[W10a]	$\cdots$	$\cdots$	283 ± 28^{ir}	W10a‡	$\cdots$
152	-/140	0.0	$\cdots$	22.3	$\cdots$	$\cdots$	$\cdots$	341 ± 19	$\cdots$	483 ± 27^{sd}	<9.10	7214–7676
153	1/-	39.9	156	10.3	18.1	2.0	$[339 \pm 13]$	$\cdots$	$\cdots$	$[250 \pm 71]^{ir}$	$10.19 \pm 0.02^{\dagger}$	7540–7860
154	-/100	42.5	$\cdots$	9.4	$\cdots$	$\cdots$	$[71 \pm 143]$	113 ± 10	$\cdots$	160 ± 14^{sd}	8.80 ± 0.11	2934–3588
155	100/-	57.2	41	33.2	42.0	8.1	W10a	$\cdots$	$\cdots$	64 ± 10^{ir}	W10a	$\cdots$
156	100/100	62.1	98	16.3	31.8	2.9	W10a	$\cdots$	$\cdots$	129 ± 9^{nr}	W10a	$\cdots$
157	-/100	33.4	$\cdots$	19.8	$\cdots$	$\cdots$	$\cdots$	164 ± 11	$\cdots$	231 ± 16^{sd}	<8.24	3981–4234
158	140/140	42.5	80	19.2	47.6	2.8	W10a	75 ± 7^{l}	$\cdots$	134 ± 18^{ir}	W10a	$\cdots$
159	68/-	75.8	28	7.4	22.7	47.4	W10a	$\cdots$	$\cdots$	93 ± 6^{nr}	W10a	$\cdots$
160	29/-	68.0(0.0)	61	10.7	22.7	16.4	W10a	$\cdots$	$\cdots$	92 ± 7^{nr}	W10a	$\cdots$
161	68/75	56.9	93	17.5	34.0	3.4	[W10a]	44 ± 7^{l}	$\cdots$	122 ± 15^{ir}	W10a‡	$\cdots$
162	80/-	66.6	19	11.6	17.0	10.6	W10a	$\cdots$	$\cdots$	38 ± 3^{nr}	W10a	$\cdots$
164	60/-	46.8	110	12.7	22.7	3.7	279 ± 7	$\cdots$	$\cdots$	192 ± 37^{nr}	9.98 ± 0.02	6240–7040
165	55/54	50.6	[119]	35.4	45.4	2.5	W10a	75 ± 8^{l}	$\cdots$	195 ± 14^{nr}	W10a	$\cdots$
166	100/-	27.9	22	10.6	17.0	9.8	123 ± 5	$\cdots$	$\cdots$	$[132 \pm 66]^{nr}$	8.76 ± 0.02	2310–2650
167	159/140*	54.7	256	18.5	26.1	1.9	544 ± 6	181 ± 12^{l}	$\cdots$	333 ± 31^{nr}	9.97 ± 0.03	8400–9100
168	80/75	66.1	180	11.8	29.5	1.6	W10a	100 ± 10^{l}	157	199 ± 21^{ir}	W10a	$\cdots$
170	12/-	42.5	92	17.4	34.0	3.0	W10a	$\cdots$	$\cdots$	187 ± 27^{nr}	W10a	$\cdots$
171	140/140	32.0(42.5)	[71]	13.2	15.9	17.9	W10a	$\cdots$	$\cdots$	$[161 \pm 40]^{nr}$	W10a	$\cdots$
172	94/100	26.4	44	6.0	18.1	11.2	194 ± 5	98 ± 9	$\cdots$	139 ± 13^{sd}	9.52 ± 0.02	4249–4524
173	-/100	45.6	$\cdots$	6.9	$\cdots$	$\cdots$	$\cdots$	205 ± 14	$\cdots$	290 ± 20^{sd}	<9.07	11987–12387
174	66/66	46.3	173	20.2	45.4	3.5	W10a	133 ± 10^{l}	$\cdots$	270 ± 31^{nr}	W10a	$\cdots$
175	177/178	78.0	101	10.9	15.9	2.4	$\cdots$	34 ± 13^{l}	$\cdots$	112 ± 12^{ir}	$<8.40^{k}$	2115–2354
176	-/140	33.0	$\cdots$	16.7	$\cdots$	$\cdots$	$[113 \pm 15]$	314 ± 18	$\cdots$	444 ± 26^{sd}	$8.77 \pm 0.08^{\dagger}$	5880–6088
177	140/140	45.6	$\cdots$	17.1	$\cdots$	$\cdots$	W10a	189 ± 11	$\cdots$	267 ± 16^{sd}	W10a	$\cdots$
178	-/2	81.2	$\cdots$	10.8	$\cdots$	$\cdots$	W10a	134 ± 9	182	203 ± 19^{sr}	W10a	$\cdots$
179	140*/-	0.0	99	20.1	30.6	3.5	W10a	$\cdots$	$\cdots$	$\cdots$	W10a	$\cdots$
180	1/2	49.5	[238]	19.0	7.9	3.8	$\cdots$	236 ± 14^{l}	163	$[333 \pm 20]^{sd}$	<9.47	10039–10631
181	44*/45*	40.0(0.0)	32	7.0	10.2	5.5	[W10a]	38 ± 14^{l}	$\cdots$	$[71 \pm 11]^{ir}$	W10a‡	$\cdots$
182	-/20	47.4	$\cdots$	18.8	$\cdots$	$\cdots$	[W10a]	268 ± 15	$\cdots$	379 ± 22^{sd}	W10a‡	$\cdots$
183	145/145.1	49.5	79	9.9	15.9	2.8	W10a	28 ± 7^{l}	68	117 ± 36^{ir}	W10a	$\cdots$
184	88/90	74.2	151	24.8	53.3	2.9	W10a	82 ± 10^{l}	146	171 ± 18^{sr}	W10a	$\cdots$
185	153/153	67.2	167	12.6	21.5	4.9	W10a	124 ± 9	$\cdots$	184 ± 21^{ir}	W10a	$\cdots$
186	10/-	61.0	110	50.6	73.7	9.1	W10a	$\cdots$	$\cdots$	134 ± 11^{ir}	W10a	$\cdots$
187	90/90	57.0(42.5)	101	5.5	7.9	2.8	$[196 \pm 7]$	78 ± 13^{l}	104	145 ± 19^{sr}	$9.65 \pm 0.03^{\dagger}$	5605–5846
188	-/90*	0.0	$\cdots$	28.1	$\cdots$	$\cdots$	$\cdots$	275 ± 16	$\cdots$	389 ± 22^{sd}	$<9.42^{k}$	7233–7611
189	45/45	25.2	91	17.9	30.6	2.2	W10a	45 ± 12^{l}	$\cdots$	$[236 \pm 109]^{ir}$	W10a	$\cdots$
190	79/90*	82.4	146	24.4	62.4	3.1	W10a	66 ± 9^{l}	$\cdots$	155 ± 5^{nr}	W10a	$\cdots$
191	90*/90*	37.8	74	15.0	22.7	13.8	W10a	182 ± 12	$\cdots$	258 ± 16^{sd}	W10a	$\cdots$
192	158/158.1	78.0	153	22.4	38.6	1.6	W10a	70 ± 7^{l}	154	177 ± 18^{sr}	W10a	$\cdots$
193	158*/158*	23.1	88	10.5	21.5	3.4	W10a	85 ± 9^{l}	$\cdots$	$[303 \pm 129]^{nr}$	W10a	$\cdots$
194	-/90*	31.7	$\cdots$	18.4	$\cdots$	$\cdots$	W10a	297 ± 17	$\cdots$	420 ± 25^{sd}	W10a	$\cdots$
195	94/94	79.9	216	28.3	49.9	5.7	W10a	127 ± 13^{l}	$\cdots$	219 ± 11^{ir}	W10a	$\cdots$

7

Table 2
(Continued)

ID	P.A.[a] (°)	i[b] (°)	V_{pmm}[c] (km s^{-1})	r_e[d] ($''$)	Extent ($''$)	Asym. (%)	W_{50}[e] (km s^{-1})	$\sigma_{r_{e/4}}$ (km s^{-1})	V_*[f] (km s^{-1})	V[g] (km s^{-1})	log $M_{\rm HI}$[h] (log $M_\odot$)	H I Range[j] (km s^{-1})
196	113/110	66.1	115	9.7	19.3	9.1	[W10a]	77 ± 30^l	...	134 ± 16^{ir}	W10a‡	...
197	-/180	44.5	...	12.9	...	...	...	231 ± 14	...	326 ± 20^{sd}	<8.69	6741–7183
198	12/20	73.2	73	32.4	61.2	11.2	W10a	...	...	88 ± 10^{ir}	W10a	...

Notes.

[a] Slit P.A.s of observations used to derive ionized gas rotation curve and stellar absorption line kinematics, respectively.

[b] Parentheses indicate inclination estimates from KFF, usually inferior except for UGC 9562 and NGC 3499, for which the new estimate applies only to the gas, not the stars.

[c] Bracketed numbers denote unreliable velocities (Section 2.1.3). Uncertainties on V_{pmm} are set to 11 km s^{-1} following KFF (Section 2.1.3).

[d] Half-light radius in the B band from Jansen et al. (2000b), converted from the authors' geometric mean aperture radius convention to a major axis radius convention. This B-band radius is denoted r_e as distinct from the r-band half-light radius denoted r_{50}^r in Table 1.

[e] Bracketed numbers denote unreliable linewidths (Section 2.1.3).

[f] Uncertainties in V_* are set to 17 km s^{-1} (Section 2.1.3).

[g] Bracketed numbers denote unreliable linewidths.

[h] Mass includes factor of 1.4 to account for He.

[j] Range of heliocentric velocities used in the H I flux measurement or upper limit determination.

[k] H I data from ALFALFA survey, with upper limits estimated from the survey sensitivity limit (Haynes et al. 2011).

[l] Stellar velocity dispersion may be an unreliable metric of characteristic velocity V, based on either late-type morphology or low dispersion (Section 2.1.3).

[*] P.A. uncertain or slit P.A. misaligned by more than $10°$ with the galaxy major axis.

[†] Confirmed likely confused; H I flux corrected as described in Section 2.1.2 and H I linewidth designated as unreliable.

[‡] Literature H I data possibly subject to confusion based on identification of a close companion or ongoing interaction/merger by KFF.

[††] Linewidth inconsistent with much larger ALFALFA value; both come from low-S/N ($\sim$6) spectra and are inconsistent with the Tully–Fisher relation.
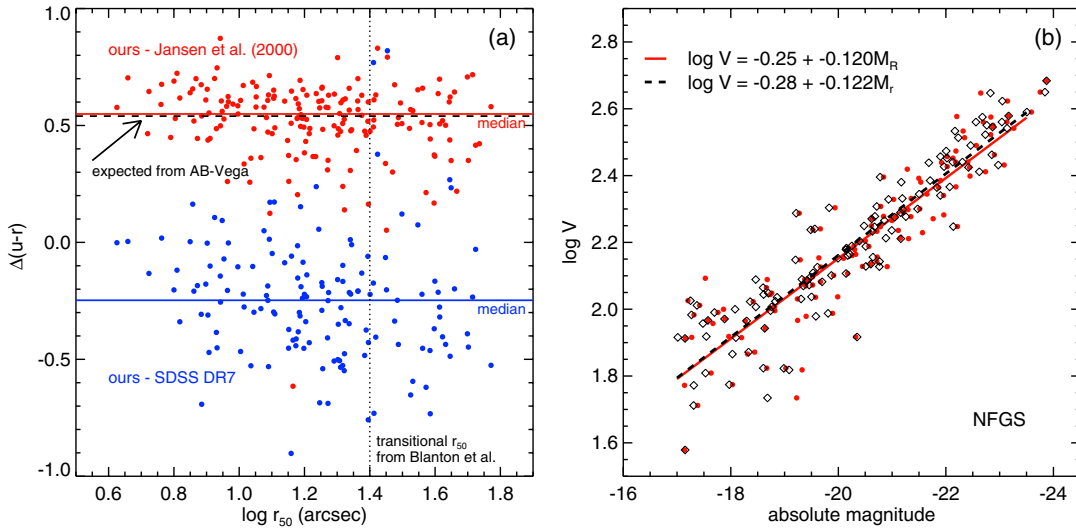
Figure 2. Comparisons of photometric and kinematic data for the NFGS. (a) Our newly measured $u - r$ colors compared to catalog $u - r$ colors from SDSS DR7 (Abazajian et al. 2009) and $U - R$ colors from Jansen et al. (2000b), as a function of R-band half-light radius (converted from the $\sqrt{ab}$ convention of Jansen et al. to a major-axis convention). Our colors are in excellent agreement with those of Jansen et al. after allowing for the known 0.04 mag AB offset of SDSS u and the 0.58 mag expected offset from Vega-to-AB conversions ($m_{Vega,AB}$ of 0.79 and 0.21 for U and R, respectively; see Blanton & Roweis 2007). The disagreement with SDSS catalog colors likely reflects (1) our use of the improved sky subtraction of Blanton et al. (2011), which those authors find to give bluer colors for log $r_{50} \gtrsim 1.4$; (2) the existence of color gradients, which are included in our photometry and that of Jansen et al. but forcibly set to zero by the SDSS model magnitude algorithm; and (3) catastrophic errors in the SDSS pipeline, contributing to the large scatter, including five extreme outliers outside the plot bounds, all with blue offsets $\Delta(u - r) < -1$. (b) Characteristic velocity V (rotation speed or $\sqrt{2}\times$ stellar dispersion σ; see Section 2.1.3) vs. M_r and M_R. Lines show forward fits minimizing residuals in V with coefficients as indicated. The close coincidence of zero points is spurious, reflecting the canceling effects of the 0.21 mag Vega-to-AB conversion for R and the $\sim$0.2 mag across-the-board zero-point difference between the Jansen et al. UBR photometry and our own (see footnote 17). Both M_r and M_R include foreground extinction and k-corrections but omit internal extinction corrections.

(A color version of this figure is available in the online journal.)

fits both the spectral energy distribution (SED) and the integrated spectrum (if available) of a galaxy with a suite of composite stellar population models. The code combines old+young simple stellar populations (SSPs) from Bruzual & Charlot (2003) in a grid of models with varying age, metallicity, and percentage of young stars. The models allow for 11 different extinction/reddening values ($\tau_V = 0, 0.12, 0.24, \ldots, 1.2$) applied to the young SSP using the Calzetti (2001) dust law. Likelihoods and

stellar masses are computed for all models in the grid, and the median of the likelihood-weighted stellar mass distribution provides the most robust final stellar mass estimate, with uncertainties determined from the 68% confidence interval around the median.

In the present work we consider two different model grids. The first, also used by S13, assumes a "diet" Salpeter initial mass function (IMF; Bell et al. 2003). It combines an old SSP

(age 1.4, 2.5, 3.5, 4.5, ..., 13.5 Gyr) with a young SSP (age 5, 25, 100, 290, or 1000 Myr), with the younger component contributing 0%, 1%, 2%, 4%, 8%, 16%, 32%, or 64% of the mass. This grid differs from that of KGB only in adding a young population age of 5 Myr. We note also that although not stated explicitly in KGB, the code *does* allow a "middle-aged" young population, i.e., one with any of the "old" ages younger than the designated old population age (for example, 2.5 Gyr combined with 13.5 Gyr). We compensate for the overrepresentation of $\lesssim 1$ Gyr SSPs in old+young pairings by downweighting the likelihoods for these pairings such that all $\lesssim 1$ Gyr SSPs together have equal weight to one "middle-aged" population option, approximating a uniform prior on the age of the younger component. Following KGB, this model set includes three metallicities $Z = 0.008$, 0.02, and 0.05 (solar/2.5, solar, and solar $\times$ 2.5).

The second model grid is our primary one for the present work. It is designed to enable estimation of the ratio of stellar mass formed within the last Gyr to preexisting stellar mass (where this ratio equals the long-term fractional stellar mass growth rate, $FSMGR_{LT}$) and therefore includes both single-burst and continuous SFH options for the young population. To facilitate comparison with the work of Salim et al. (2007, hereafter S07) in Section 4.2, our model grid emulates theirs in including an additional low-metallicity choice ($Z = 0.004$) and adopting a Chabrier IMF. We further consider that even continuous star formation can be bursty on ~ 200 Myr timescales (e.g., Weisz et al. 2012), which S07 choose to model with superposition of random bursts. To keep the grid size manageable, since only the most recent bursts are likely to strongly affect the model fits, we take the alternative approach of constructing a set of young population models that have constant star formation running from 1015 Myr ago to a turn-off point sometime between 0 and 195 Myr ago, sampled every 15 Myr. The young population options also include 5 models representing quenching bursts without subsequent star formation: SSPs with ages 360, 509, 641, 806, and 1015 Myr. For computational convenience, we restrict the old SSP choices in this model grid to six ages (2, 4, 6, 8, 10, and 12 Gyr). However, we now consider 13 young stellar population mass fractions (0.001, 0.002, 0.005, 0.011, 0.025, 0.053, 0.112, 0.220, 0.387, 0.585, 0.760, 0.876, 0.941), equally spaced logarithmically in $FSMGR_{LT}$. Once again, an old SSP can serve as the younger model in an old+young pair, and $FSMGR_{LT} = 0$ in such a case. The overrepresentation of pairings with young age $\lesssim 1$ Gyr is approximately canceled by downweighting the likelihoods for these models, where we treat all of the continuous SFH models together as having combined weight equal to one of the five $\lesssim 1$ Gyr bursts and then further downweight both types of young models relative to the "middle-aged" SSPs to approximate a uniform prior on the age of the younger component.

As data are available, we simultaneously fit these model grids to NUV+$ugrizJHK$+IRAC 3.6 μm SEDs as well as optical spectroscopy. We apply the 0.04 mag AB offset for the u band[17] inside the code. To the individual magnitude errors we add extra photometric uncertainties to account for variations between methods of foreground extinction correction and sky level estimation: 0.1 mag in the NUV, 0.05 mag in u, 0.03 mag in $griz$, and 0.1 mag in JHK+IRAC 3.6 μm, with an extra 0.1 mag in JHK for faint blue galaxies (M_r or $M_R > -19$ and $u-r < 1.4$ or $U - R < 0.7$). These choices are motivated by the analyses

of Abazajian et al. (2004), Morrissey et al. (2007), and Blanton et al. (2011), as well as our own analysis of the agreement of our JHK magnitudes with the best fits. When SDSS data are unavailable, we substitute the UBR magnitudes from Jansen et al. (2000b), applying a uniform 0.2 mag offset to reconcile the UBR zero points with our brighter SDSS magnitudes, where this offset value is estimated by fitting both $ugriz$ and UBR simultaneously when possible in an initial round of SED fits. Our final fits do not include UBR when we have $ugriz$, however, to minimize systematics. We note that our estimated across-the-board ~ 0.2 mag offset is opposite to the Vega-to-AB offset for the R band and thus yields fortuitous zero-point agreement between the r and R bands (as seen, for example, by comparing the merged NFGS Tully–Fisher/Faber–Jackson relations shown in Figure 2; see Section 2.1.3).[18]

Stellar masses estimated with the second model grid are provided in Table 1. With so many independent data points, these mass estimates are quite robust; estimates derived using the first model grid are offset 0.1 dex higher than those derived using the second model grid but otherwise agree within 0.1 dex rms (less than the typical uncertainty of 0.15 dex from the stellar mass distributions). The only obviously unreliable case is UGC 4879, an extremely nearby system for which our photometry is notably inconsistent, possibly due to the technical difficulty of sky subtraction or to a complex post-starburst SED (the same galaxy lacks any emission or absorption features and thus also defies kinematic analysis). For reference, Table 1 also provides the stellar masses previously derived by KGB using a model set very similar to our first model grid, but with inferior photometry (uncorrected UBR + catalog 2MASS data); these masses show 0.2 dex scatter and +0.06 dex median offset relative to our preferred masses. We include the KGB masses because they have been used in several recent papers (Wei et al. 2010a, 2010b; Moffett et al. 2012) and compared to stellar masses from Kauffmann et al. (2003b); this comparison demonstrates similar stellar-mass zero points (Kannappan & Wei 2008).

To ensure uniform color data, we use our stellar population model fits to interpolate likelihood-weighted $(u - r)^m$ and $(u - J)^m$ colors for all galaxies, regardless of the availability of these specific bands, where the superscript m is a reminder that these colors come from the models and thus include the AB correction to the u band as well as k-corrections to $z = 0$. Self-consistent internal extinction corrections can also be determined with our newer model grid, enabling us to examine the behavior of the de-extincted colors, denoted $(u - r)^e$ and $(u - J)^e$.

Half-light and 90% light radii are also given in Table 1, as these radii are used to compute μ_Δ, a new quantitative morphology metric introduced in this work to facilitate comparison of the NFGS and V3000 samples. We define μ_Δ as

$$\mu_\Delta = \mu_{90} + 1.7\Delta\mu \qquad (1)$$

---

[17] http://www.sdss.org/dr7/algorithms/fluxcal.html#sdss2ab

[18] Applying the sky subtraction technique described in Jansen et al. (2000b) to SDSS DR8 images (which are pre-sky-subtracted using the methods of Blanton et al. 2011) reveals that ~ 0.1 mag of the offset we measure is probably due to oversubtraction of sky by Jansen et al. compared to the new protocol (as expected from Figure 12 of Blanton et al.). The remainder may be partly due to a mismatch between the UBR filter systems used in our stellar population fitting code and used by Jansen et al., and/or partly due to differing profile extrapolation techniques. Regarding the latter, we note that the zero-point discrepancy increases for low surface brightness galaxies, in the sense that our reprocessed SDSS magnitudes are brighter and the spurious agreement between the V–M_r/M_R relations in Figure 2 becomes tighter.

combining an overall surface mass density

$$\mu_{90} = \log \frac{0.9 M_*}{\pi r_{90,r}^2} \qquad (2)$$

with a surface mass density contrast

$$\Delta\mu = \log \frac{0.5 M_*}{\pi r_{50,r}^2} - \log \frac{0.4 M_*}{\pi r_{90,r}^2 - \pi r_{50,r}^2} \qquad (3)$$

representing the difference between the surface mass densities within the 50% light radius and between the 50% and 90% light radii, where all radii are converted to physical kiloparsec units. The 1.7 multiplier helps to separate quasi-bulgeless, bulge+disk, and spheroid-dominated types as illustrated in Figure 1(b), yielding approximate divisions at $\mu_\Delta = 8.6$ and 9.5 as shown. For galaxies without $r_{50,r}$ measurements, we use the R-band half-light radii from Jansen et al. (2000b), converted from the authors' geometric mean aperture radius convention to a major axis radius convention. We find a one-to-one correspondence between the r- and R-band half-light radii, with rms scatter $\lesssim 15\%$ and a small 3.3% offset, in the sense of larger r-band radii. When using $r_{50,R}$ we assume the median value of $r_{90,r}/r_{50,r} = 2.6$ to infer $r_{90,R}$.

2.1.2. Gas Masses and H I Linewidths

The H I data set presented in Table 2 expands on that of Wei et al. (2010a, hereafter W10a) with 30 new Robert C. Byrd Green Bank Telescope (GBT) 21 cm observations taken for the NFGS under program GBT10A-070 in 2010 January, February, and July (PI: Kannappan). We add these to the 27 GBT observations obtained by W10a under programs GBT07A-072 and GBT07C-148 in 2007 March and October. We have reprocessed the W10a data along with our new data since discovering that the default GBTIDL flux calibration, which was used by W10a, is ~15%–20% lower than that obtained from the observed flux calibrators, and also since finding an error in how W10a estimated rms noise during linewidth measurement, which led to overestimation of linewidths by $\gtrsim 10\%$. Other than these adjustments, our flux and linewidth measurements follow the methods of W10a closely for unconfused detections. In particular, we do not correct for self-absorption, which is expected to alter total H I flux estimates by <30%, even for the most inclined systems (Giovanelli et al. 1994). Note that the masses denoted $M_{\rm H\,I}$ in Table 2 and the rest of this paper are measured directly from 21 cm fluxes using the equation $M_{\rm H\,I} = 1.4 \times 2.36 \times 10^5 f_{\rm H\,I}(cz/H_0)^2 M_\odot$, which combines the expression from Haynes & Giovanelli (1984) with a $1.4\times$ correction factor for He.

For non-detections and/or galaxies confused with companions in the beam, we have adopted a slightly different approach than W10a in our definition of integration bounds for estimating 3σ upper limits and for dividing flux between objects. Upper limits are now calculated using the equivalent W_{20} linewidths determined either from (a) the optically derived V, where V is based on Hα or stellar rotation curves extending beyond $1.3 r_e$ (see Sections 2.1.3 and 2.1.4), or, in the absence of such data, from (b) the implied V from the R-band absolute magnitude–V relation $\log V = -0.25 - 0.120 M_R$, which has been calibrated using all galaxies with reliable V and $M_R < -17$ in the NFGS (Figure 2). Here V is estimated from either stellar or ionized gas kinematics as described in Sections 2.1.3 and 2.1.4 and is

defined to scale as $W_{50}/(2 \sin i)$ (so we adjust for an assumed offset of $W_{20} - W_{50} = 20$ km s^{-1}; see Kannappan et al. 2002). We also account for the projection factor $\sin i$, adopting a minimum i of 30° for E galaxies to avoid overly strong upper limits, given the lack of reliable inclination information for such round objects. Likewise, we avoid overly strong upper limits for face-on disks by employing a minimum final integration linewidth of 40 km s^{-1} reflecting non-rotational line broadening. These definitions ensure that we compute conservative upper limits.

We have confirmed 11 cases of profiles confused with companion galaxies in our GBT data from a thorough search within twice the GBT half-power beam diameter of 9′, assuming typical redshift uncertainties and linewidths and inspecting each of the 15 potential cases by eye. To isolate the flux for the primary target, we typically assign the primary all flux within the equivalent W_{50} linewidth derived from the measured or inferred V as discussed above, omitting the offset to the W_{20} scale. Alternatively, if one half of the profile is obviously more contaminated, we integrate the uncontaminated half and double that flux. In the case of UGC 12265N, which is strongly interacting with a similar size companion and thus more severely confused than usual, W10a employ a Very Large Array 21 cm map to determine that only ~25% of the flux belongs to the target galaxy, and we retain this flux division. Our flux separations are validated by the absence of significant outliers in our analysis (see especially Section 4.1).

Table 2 summarizes the final derived GBT $M_{\rm H\,I}$ values/uncertainties or 3σ upper limits, plus linewidths and velocity integration ranges. For galaxies that share the beam with one or more companions, linewidths represent the full H I profiles not deblended to account for confusion. Confused linewidths are thus enclosed in brackets to indicate that they are unreliable. Likewise, linewidths derived from profiles with peak S/N < 6 are bracketed. Linewidth uncertainties are estimated using $\sigma_{W_{50}} = 4.1(P/({\rm S/N}))^{0.85}$, where P is the steepness parameter defined as $P = (W_{50} - W_{20})/2$ (this formula is derived as in S13 but assuming 5 km s^{-1} spectral resolution; see S13 for further details).

We have further augmented the 21 cm inventory for the NFGS using the literature compilation of W10a (not duplicated in Table 2) and the ALFALFA survey (Haynes et al. 2011). In particular, one detection and four upper limits inferred from ALFALFA are given in Table 2, with the upper limits estimated using the median rms noise as a function of declination (typically ~2.3 mJy; Haynes et al. 2011). Unlike our GBT upper limits, ALFALFA upper limits are determined at 5σ, matching the survey detection threshold. The literature compilation of W10a includes the remaining 128 galaxies, so together, these data sets yield $M_{\rm H\,I}$ values or upper limits for all 190 galaxies in the sample, with only 1 of the 26 upper limits weaker than 10% of that galaxy's stellar mass (Section 2.1.1). As it is infeasible to uniformly assess and decompose confusion in the literature H I measurements, we have simply flagged likely cases of confusion in literature data based on the presence of a companion, interaction, or merger identified by Kannappan et al. (2002); such cases are marked in Table 2.

Molecular gas data are not uniformly available for the NFGS, but we have made use of 39 CO-derived H$_2$ masses tabulated in Wei et al. (2010b) and/or in S13 to determine that including molecular gas in the total gas inventory has negligible impact on our conclusions except to reinforce them. The effect of molecular gas is illustrated in several figures in Sections 3 and 4, always with a $1.4\times$ correction factor for He.

2.1.3. Optical Kinematics

Ionized gas and stellar rotation velocities and stellar velocity dispersions for the NFGS are also given in Table 2. These measurements are based on emission- and absorption-line observations previously reported in Kannappan et al. (2002, hereafter KFF) and Kannappan & Fabricant (2001), coming from either the FAST Spectrograph on the Tillinghast telescope or the Blue Channel Spectrograph on the MMT telescope. For stellar dispersions σ, the instrumental resolution is at least $\sigma_{instr} \sim 60$ km s^{-1} at the Mg I triplet near 5175 Å, improving to ~ 40 km s^{-1} for the MMT data. We tabulate the stellar dispersion $\sigma_{r_{e/4}}$ measured within one-fourth the B-band half-light radius r_e. Comparison of dispersions derived with various template star spectra (broadened and shifted to match the galaxy spectrum using the Fourier-space fitting code of van der Marel & Franx 1993) indicates $\sim 5\%$ systematic errors, which we convolve into the reported uncertainties. For ionized gas rotation velocities, we adopt a non-parametric statistical estimator of the maximum rotation velocity, the "probable min–max" V_{pmm} of Raychaudhury et al. (1997) as implemented in KFF. The raw error for V_{pmm} is set to the 11 km s^{-1} systematic uncertainty estimated by KFF from comparison to radio linewidths (scaled from the 20 km s^{-1} scatter in the conversion $W_{50} = 33 + 0.92(2V_{pmm})$ from KFF's Appendix B3). Stellar rotation velocities V_* are also available for some galaxies, where we have applied the probable min–max technique to a rotation curve extracted with the IRAF cross-correlation task xcsao (Kurtz et al. 1992). Table 2 also provides the extent and asymmetry of the gas rotation curves (see Kannappan & Barton 2004), as well as the slit P.A.s for both gas and stellar observations, with an asterisk in case the slit alignment with the galaxy major axis is uncertain or misaligned by more than $\sim 10°$. Comparisons using (1) different instrumental setups and (2) different rotation curve extraction techniques indicate that both asymmetry and V_{pmm} measurements are quite repeatable for rotation curves of reasonable S/N (Barton et al. 2000; Kannappan & Barton 2004), while extent measurements are somewhat more dependent on S/N.

Values of V_{pmm} may be bracketed as unreliable in Table 2 if the ionized gas rotation curve is unlikely to adequately probe the potential well due to limited radial extent (e.g., Pisano et al. 2001; Kannappan & Barton 2004). For morphological types earlier than Sc, a reliable rotation curve is defined to extend past $1.3r_e$ (using the average extent of the two sides), which corresponds to the canonical turnover radius for large spiral galaxy rotation curves (KFF). For types Sc or later, we relax this criterion slightly in requiring only extent $>r_e$, because rotation curves that do not turn over are typical for very late-type galaxies and do not generally yield low-V outliers in the Tully–Fisher relation. No values of stellar σ are bracketed in Table 2 because data with inadequate S/N or resolution to obtain reliable σ values are not reported; likewise, we do not report V_* when the stellar rotation curve extends to $<1.3r_e$. Although all stellar kinematic measurements we report should therefore be reliable, dispersions marked with an l should be used cautiously as dynamical mass estimators, due to the likelihood of substantial rotational support not accounted for in the stellar σ alone (see the next section).

2.1.4. Characteristic Velocity Assignments and Inclinations

For each galaxy, we assign the largest reliable velocity derived from either gas or stellar kinematics as the characteristic internal velocity V listed in Table 2. In principle V should be equal to the inclination-corrected gas rotation velocity for an idealized, purely dynamically cold system. Because in practice gas turbulence and other non-circular motions included in H I linewidths contribute to the dynamical support of galaxies, we adopt the inclination-corrected H I linewidth $W_{50}/(2\sin i)$ as our fiducial gas-derived V, converting the ionized-gas V_{pmm} to a pseudo-W_{50} via the empirical optical–radio calibration in KFF. This approach restores non-rotational gas support to our ionized-gas-derived V estimates in an average way (and is validated by the tighter Tully–Fisher relation obtained by Kassin et al. 2007 when they explicitly measure and include ionized gas dispersion for a high-redshift galaxy sample). To put stellar V_* measurements on the same scale, we first multiply them by 1.1 (the typical V_{pmm}/V_* ratio measured in cases where both rotation curves extend to $>1.3r_e$) and then scale them just like ionized gas V_{pmm} measurements.

We further attempt to put rotation- and dispersion-derived estimates of V on the same scale by applying the rule that for a pure dynamically hot system, V equals $\sqrt{2} \times$ the stellar σ (an approximation based on the scaling for an isothermal sphere; Burstein et al. 1997). However, low-mass E/S0 galaxies may be significantly supported by stellar rotation (Davies et al. 1983), and we cannot assess this support uniformly with the data in hand. In several cases, gas or stellar rotation curves confirm substantial rotational support, generally yielding strong outliers from the Faber–Jackson relation below $V \sim 125$ km s^{-1} (Section 3). Thus, we consider stellar dispersion-derived V values unreliable for E–S0a galaxies with $V < 125$ km s^{-1}, except for two that are clearly dynamically hot, with dispersions consistent with the Faber–Jackson relation for high-mass galaxies (NGC 3605 and NGC 4308). For the same reason we consider stellar dispersion-derived V values unreliable for galaxies of type Sa or later. We mark low-mass/late-type σ measurements with an l in Table 2 to indicate likely unreliability. However, if such a σ exceeds a *reliable* gas-derived V, then we accept the stellar-derived V as reliable.

Superscripts *ir, nr, sr,* and *sd* indicate the origin of the final V estimates in Table 2 from ionized-gas rotation V_{pmm} (79 galaxies), neutral gas rotation W_{50} (53 galaxies), stellar rotation V_* (12 galaxies), or stellar dispersion $\sigma_{r_{e/4}}$ (47 galaxies), where 24, 17, 2, and 8 of the final V values in each category are bracketed as unreliable, respectively, leaving 140 reliable final V values. In combining the four types of kinematic data, we adopt two additional unreliability criteria besides those detailed in Sections 2.1.2 and 2.1.3: (1) although we assume that H I W_{50} measurements probe the full potential well for late-type galaxies, for types S0a and earlier we consider the H I W_{50} measurement unreliable if the ionized gas rotation curve is truncated, based on experience that H I in S0s often fails to probe the full potential well (KFF); and (2) for rotation-derived V values, we treat the inclination correction as reliable only for $i > 40°$.

Our current best inclination angle estimates are provided in Table 2, mostly derived from photometric axial ratios as in KFF. A few values have been updated, with the old values used by KFF given in parentheses. For the polar ring galaxy UGC 9562 we adopt $i = 68°$ for the gas ring based on interferometric CO data (Wei et al. 2010b), and similarly for NGC 3499 we adopt $i = 90°$ for the gas (but not the stars) given the appearance of an edge-on dust lane in an otherwise round system. For NGC 7077 we list the $i = 40°$ inclination estimate from Wei et al. (2010b) for the record, although it just misses our inclination cut so the change does not affect our analysis. For UGC 6206 we adopt $i = 43°$ as a compromise between the highly discrepant
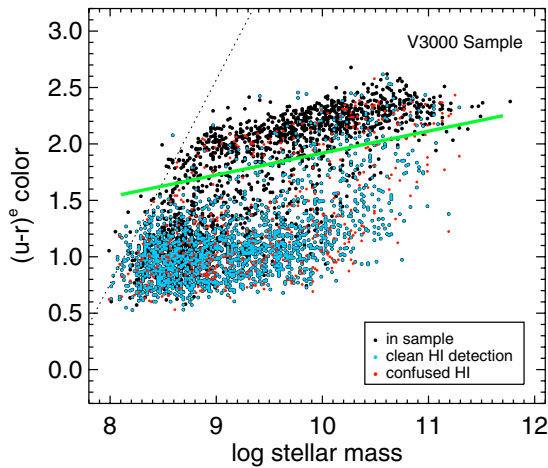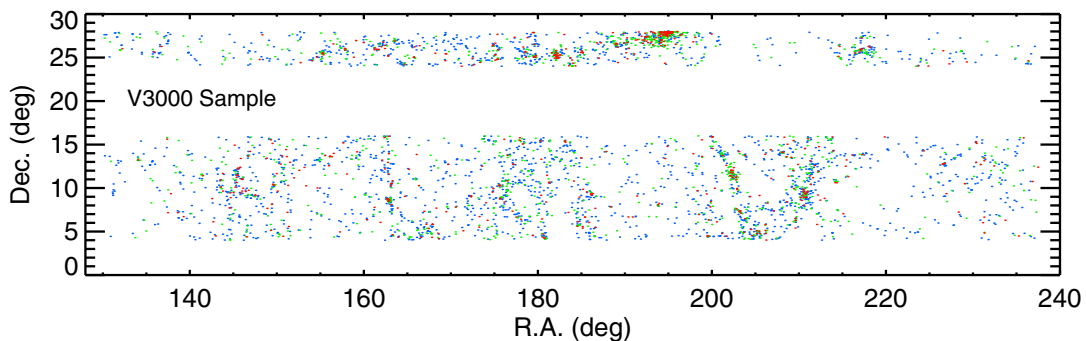
Figure 3. V3000 sample shown in $(u - r)^e$ color vs. stellar mass parameter space. As in Figure 1, we use de-extincted colors to enhance separation of the sequences. Galaxies with unconfused H I detections (blue dots) lie primarily on the blue sequence. Red dots mark possibly confused H I detections, which are excluded from the remainder of our analysis. The obviously slanting selection effect marked by the dashed line at the low-mass end of the plot reflects the fact that the *r* band used to define the sample correlates most directly with *baryonic* rather than stellar mass, as shown in Figure 5 (see also Kannappan & Wei 2008).

(A color version of this figure is available in the online journal.)

axial ratios quoted by Mazzarella & Boroson (1993) and Jansen et al. (2000b). For UGC 12265N, which has a very small angular size, the Jansen et al. axial ratio would be calculated with too few significant digits to give a meaningful constraint on the inclination, so we use the axial ratio from the NASA Extragalactic Database to estimate $i = 57°$. Finally, for the strongly distorted galaxy NGC 5993 we reduce the inclination to $i = 32°$ based on our analysis of the SDSS photometry (implying $i < 40°$ or "unreliable" status, consistent with this galaxy's extreme Tully–Fisher outlier behavior discussed in KFF).

2.2. The V3000 Sample

The V3000 sample spans a redshift range of 2530–7000 km s^{-1} within two SDSS sky regions that offer uniform, public H I data from the blind 21 cm ALFALFA survey in the α.40 data release (R.A. 130°–237°.5, decl. 4°–16° and 24°–28°; Haynes et al. 2011). Including all galaxies known to be in the volume down to $M_r = -17$, the sample comprises 3834 galaxies, not including 57 galaxies with irretrievable photometry (usually due to a missing/corrupted SDSS image or a very bright star). Of these,

1911 have clean H I detections, 1527 have H I upper limits, and 396 have possibly confused H I detections. The distribution of H I data in the color versus stellar mass diagram for the V3000 sample is shown in Figure 3. The high rate of upper limits ($\sim$40%) is obviously unsatisfying, but increasing the survey volume toward redshifts <2500 km s^{-1} in order to add more detections would present substantial challenges for robust photometry and stellar mass estimation, while adding a modest number of galaxies and introducing a strong bias toward the Virgo Cluster. As defined, the V3000 sample reflects the natural diversity of galaxy environments ranging from voids to clusters (Figure 4).

The V3000 sample has been designed as a superset of a sample that would be complete to a limiting baryonic mass of $\sim$10$^{9.3}$ $M_\odot$, allowing for variable mass-to-light ratio. The *r* band is optimal for selection on baryonic mass due to the modest scatter and luminosity dependence of *r*-band baryonic mass-to-light ratios (Figure 5; see also Kannappan & Wei 2008). The nominal completeness limit of the SDSS redshift survey, Petrosian $r = 17.77$ mag (using SDSS DR7 catalog magnitudes corrected for foreground extinction), corresponds to Petrosian $M_r = -17.23$ at 7000 km s^{-1}, the far side of the V3000 volume. Our extrapolated *r*-band magnitudes are systematically brighter than catalog Petrosian magnitudes by $\sim$0.1 dex (with large outliers; see Figure 5), due to improved sky subtraction and robust extrapolation (Section 2.1.1), so our equivalent limit is $M_r \sim -17.33$. We have furthermore reprocessed photometry for many galaxies near the survey limit, extending the sample down to $M_r = -17$ where redshifts are available and recovering bright galaxies shredded by the SDSS pipeline. For this effort, we have made use of a merged redshift catalog that draws on SDSS DR6/DR7/DR8, Updated Zwicky Catalog, HyperLEDA, ALFALFA, 6dF, 2dF, and GAMA data (Adelman-McCarthy et al. 2008; Abazajian et al. 2009; Aihara et al. 2011; Falco et al. 1999; Paturel et al. 2003; Haynes et al. 2011; Martin et al. 2010; Jones et al. 2009; Colless et al. 2003; Driver et al. 2011). Roughly 8% of the V3000 sample above $M_r = -17.33$ has been recovered in this way. It is worth noting that most of the extra redshifts come from historical surveys with fairly bright limiting magnitudes, so our inventory of low surface brightness dwarfs remains incomplete.

The scatter in Figure 5(a) suggests high completeness to $M_r = -17.73$, corresponding to a typical baryonic mass of $\sim$10$^{9.1}$ $M_\odot$, as shown in Figure 5(b). However, variations in baryonic mass-to-light ratio up to $\sim$3 would mandate extension to $M_r \sim -17$ to retain unbiased completeness at $M_{\rm bary} \sim$10$^{9.1}$ $M_\odot$. As we have only partial completeness from $M_r = -17$ to -17.33, we

Figure 4. V3000 sample on sky. The sample includes all known galaxies with $M_r < -17$ in the two sky regions shown, from $cz = 2530$ to 7000 km s^{-1}. It spans a naturally diverse range of environments, including part of the Coma Cluster (cut off at the top). Blue, green, and red points indicate quasi-bulgeless, bulged disk, and spheroid-dominated galaxies based on μ_Δ class (Figure 1). Points are overplotted in that order to highlight sites of spheroid-dominated galaxy concentration.

(A color version of this figure is available in the online journal.)

Figure 5. Assessing completeness for the V3000 sample. (a) Comparison of SDSS DR7 catalog Petrosian magnitudes vs. total extrapolated magnitudes from our reprocessed DR8 photometry for the V3000 sample, omitting k-corrections for direct comparison. The one-to-one line is shown for reference. (b) Translation of the approximate completeness limit from panel (a) to a typical baryonic mass of $\sim 10^{9.1} \, M_\odot$ based on NFGS r-band magnitudes obtained with the same pipeline used for the V3000 sample. Note that the r band correlates with baryonic mass better than with stellar mass, with 40% smaller logarithmic scatter ($\sigma = 0.14$ vs. 0.24 dex for galaxies with $M_r < -17$). (c) Baryonic mass-to-light ratios in the r band stay fairly flat (changing by a factor of <2 over 6 mag in M_r) and show modest 0.14 dex scatter, in contrast to the steeper slope and greater scatter seen for r-band stellar mass-to-light ratios. Thus, r-band selection approximates selection on baryonic mass; nonetheless, scatter up to mass-to-light ratios of ~ 3 implies a final baryonic mass completeness limit of $\sim 10^{9.3} \, M_\odot$.

(A color version of this figure is available in the online journal.)

estimate that the V3000 sample is complete to $M_{\rm bary} \sim 10^{9.3} \, M_\odot$ and $M_* \sim 10^{9.1} \, M_\odot$. We define an initial approximately baryonic mass limited sample by $M_r < -17.73$, which yields 3020 galaxies, of which 1510 have unconfused H I detections and 1171 have upper limits. In Section 4.4.1 we attempt to define a more precisely baryonic mass-limited sample by estimating gas content via "photometric gas fractions" (K04) for galaxies with upper limits and then selecting all galaxies with $M_{\rm gas} + M_* > 10^{9.3} \, M_\odot$ down to $M_r = -17$.

Photometric measurements for the V3000 sample have been performed as part of the ongoing construction of two other volume-limited surveys not restricted to the ALFALFA α.40 footprint (RESOLVE, REsolved Spectroscopy Of a Local VolumE; S. J. Kannappan et al., in preparation; and a larger survey encompassing both the RESOLVE and V3000 samples; A. J. Moffett et al., in preparation). These surveys will enable analysis within environmental context, which we defer to future work. We reprocess *GALEX*, SDSS DR8, and 2MASS imaging in the same way as for the NFGS (Section 2.1.1); *GALEX* imaging is available for $\sim 30\%$ of the V3000 sample. Stellar-mass estimates for the V3000 sample are derived from the NUV+$ugrizJHK$ magnitudes using the same updated model grid used to determine new mass estimates for the NFGS (Section 2.1.1). From a comparison of colors and masses for the V3000 sample and the SDSS-derived "HyperLEDA+" sample of KGB, we conclude that our new photometry and updated model grid together yield similar, slightly lower stellar masses and ~ 0.2 mag bluer $u - r$ colors than would be obtained with SDSS catalog photometry, consistent with the discussion in Section 2.1.1.

For V3000 galaxies with 21 cm detections we obtain H I fluxes and W_{50} linewidths from ALFALFA catalog measurements, implying likely underestimation of the true characteristic velocity in the case of gas-poor systems. We therefore treat W_{50} as unreliable for detections below $M_{\rm H I}/M_* = 0.1$, which rejects a large fraction of the outliers in the ALFALFA W_{50}-based Tully–Fisher

relation. Formal errors from the ALFALFA catalog typically imply $\lesssim 5$–10 km s^{-1} error on $W_{50}/(2 \sin i)$, so we treat cases with >20 km s^{-1} error as unreliable as well. In either case, when our analysis requires a velocity we use the equivalent V inferred from the r-band absolute magnitude–velocity relation $\log V = -0.29 - 0.123 M_r$ (calibrated using all galaxies with reliable V and $M_r < -17$ in the NFGS; this calibration is very slightly different from that in Figure 2 due to evolution in the photometry after the H I measurements were performed). An M_r-inferred V is also used to compute $M_{\rm H I}$ upper limits (defined at 5σ); we combine the inferred V with the measured inclination angle and the declination-dependent ALFALFA rms noise to derive the limit value as well as provide a $W_{50}/(2 \sin i)$ surrogate. Finally, because we estimate inclinations for the V3000 sample from axial ratios determined by our automated pipeline, we cannot individually vet inclination estimates in the borderline $i = 40°$–$50°$ range as we could for the NFGS, so $W_{50}/(2 \sin i)$ is designated unreliable for $i < 50°$ and again replaced with an M_r-inferred V.

Possible confusion of H I sources is flagged within a $3'$ radius, which combines the $2'$ half-power radius of the smoothed ALFALFA resolution element with another $1'$ to allow for the typical $\sim 0.'5$–$1'$ diameters of galaxies in this redshift range. We assume catalog redshift uncertainties (minimum 50 km s^{-1}) and ~ 100 km s^{-1} profile widths (the approximate average of the H I velocity width function of Papastergis et al. 2011) to assess potential overlap, employing the same merged redshift catalog described above. Potentially confused detections are excluded from our H I analysis but are shown as red dots in Figure 3.

3. DISTINGUISHING THE GAS-RICHNESS THRESHOLD AND BIMODALITY SCALES

Figure 6 combines the Tully–Fisher and Faber–Jackson relations for the NFGS into a unified mass–velocity (M–V) relation for stellar mass in panel (a) and baryonic mass in panel (b), illustrating multiple equivalent definitions of the threshold and bimodality scales in terms of V, M_*, and $M_{\rm bary}$ (stars + cold
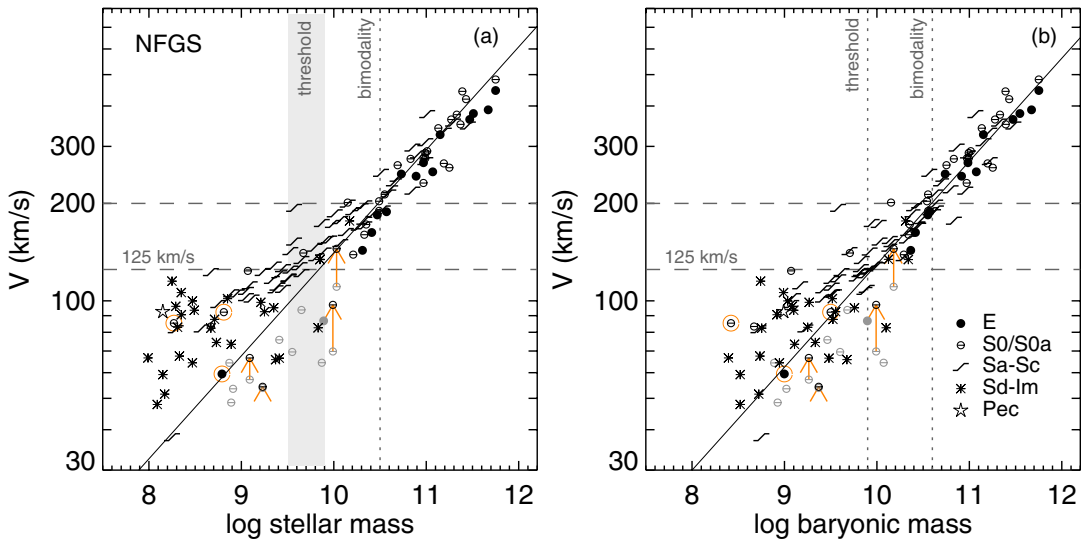
Figure 6. Combined Faber–Jackson/Tully–Fisher relation for the NFGS, plotting characteristic velocity V as in Figure 2 vs. (a) stellar mass and (b) baryonic mass (stars + neutral atomic gas). The gas-richness threshold and bimodality scales discussed in Section 3 are marked. The fit in panel (b) is performed for all galaxies above baryonic mass $M_{bary} = 10^{10} M_\odot$, minimizing residuals in V, and yields $\log V = -1.07 + 0.318 \log M_{bary}$ (implying $M_{bary} \sim V^{3.1}$). The same fit is repeated in panel (a), shifted by the ~ 0.1 dex mean mass offset for the same subsample, to highlight deviations from the M_*–V relation due to increasing gas content, especially below $V \sim 125$ km s^{-1} (Figure 7). Gray symbols indicate E/S0s whose V values computed from stellar σ values alone are treated as unreliable, due to likely mixed rotation+dispersion support. Orange arrows connect some of these to reliable V values determined from gas rotation; in the remainder of this work, the rest are given V values determined from the baryonic M–V fit to all reliable data points in panel (b): $\log V = -0.49 + 0.264 \log M_{bary}$ (implying $M_{bary} \sim V^{3.8}$). Orange circles indicate additional E/S0s with gas-derived V values, in this case with no stellar σ values for comparison.

(A color version of this figure is available in the online journal.)

gas). The characteristic velocity V used is the optimal choice of stellar or gas-derived internal velocity for each galaxy as described in Section 2.1.4. The bimodality scale corresponds to the $M_* \sim 10^{10.5} M_\odot$ scale highlighted by Kauffmann et al. (2003a), which we identify with $V \sim 200$ km s^{-1} in Figure 6. The threshold scale corresponds to the $V \sim 125$ km s^{-1} scale highlighted by Garnett (2002) and Dalcanton et al. (2004)[19], which we identify with $M_{bary} \sim 10^{9.9} M_\odot$ in Figure 6. The wide range of gas-to-stellar mass ratios at the threshold scale (Figure 7) permits no well-defined stellar mass equivalent, but a reasonable fiducial is $M_* \sim 10^{9.7} M_\odot$ in the middle of the 0.4 dex band shown.

The gas-richness threshold and bimodality scales are distinguished by simultaneous changes in structure (morphology/dynamics) and gas-richness. Figure 1(a) shows that quasi-bulgeless Sd–Im morphologies ("dwarf" late types) become notably more common below the threshold scale, while spheroid-dominated E–S0a types become similarly abundant above the bimodality scale. This pattern is consistent with previous work showing the emergence of bulges above the threshold scale (Dalcanton et al. 2004; Bell 2008) and the transition from disk-dominated to spheroid-dominated systems above the bimodality scale (Kauffmann et al. 2003a). In the NFGS, traditional Sa–Sc spirals are most prominent in the narrow mass range between the threshold and bimodality scales, but whether they numerically predominate is unclear. We defer consideration of this question to Section 4.4.3, where we will use the volume-limited V3000 sample to examine what defines the transition range between the threshold and bimodality scales.

Symbol colors in Figure 1(a) indicate quasi-bulgeless, bulged disk, and spheroid-dominated galaxies according to our μ_Δ metric (Section 2.1.1 and Figure 1(b)), which combines overall

surface mass density with central versus outer-disk surface mass density contrast. We see that below the threshold scale, most NFGS galaxies typed as spirals are quasi-bulgeless, while earlier type galaxies, particularly those on the blue sequence, often have μ_Δ comparable to that of Sa–Sc spirals. The latter result is consistent with the idea that low-mass blue-sequence E/S0s are associated with disk rebuilding after gas-rich mergers, likely leading to the regeneration of late-type morphologies (KGB; W10a; Wei et al. 2010b; Moffett et al. 2012; S13). Like spirals, S0s display the full range of μ_Δ classes (as also emphasized by the classification system of van den Bergh 1976).

E/S0s above the bimodality scale are generally dynamically hot (as judged by the fact that stellar velocity dispersions alone can provide most of the virial support required for the M–V relation[20]; Figure 6), but the E/S0 population diversifies at lower masses, with only a minority remaining dynamically hot. For E/S0s just below the bimodality scale, the scatter in dispersion-derived V estimates stays within $\sim 20\%$ of the baryonic and stellar M–V relations, but below the threshold scale, severe M–V outliers would be common if we accepted stellar σ values as reliable estimators of V (light gray symbols in Figure 6(a)). Significant rotational support most naturally explains this outlier behavior, as confirmed for a few cases that have reliable gas-derived V values (see V estimates connected with orange arrows in Figure 6(b)). In keeping with this interpretation, the low-mass E/S0s whose *only* reliable V is gas derived are not

---

[19] Dalcanton et al. adopt a slightly different $V = 120$ km s^{-1} value as compared to Garnett's 125 km s^{-1} value adopted here.

[20] It is interesting that massive S0 and early-type spiral galaxies may have photometrically prominent disks and yet still have sufficiently high stellar σ values to account for most of their virial support. Barway et al. (2007, 2009) find that lenticular galaxies above a K-band magnitude of -24.5 (which roughly equates to $M_* \sim 10^{10.8-10.9} M_\odot$; KGB) have bulges consistent with formation involving mergers rather than pure secular evolution. The final analysis of Laurikainen et al. (2010, updating their earlier papers) also confirms that lenticular galaxies above this luminosity behave more like ellipticals in the central surface brightness versus effective radius relation than like pseudobulge-dominated S0s, which are more typical at lower luminosities.
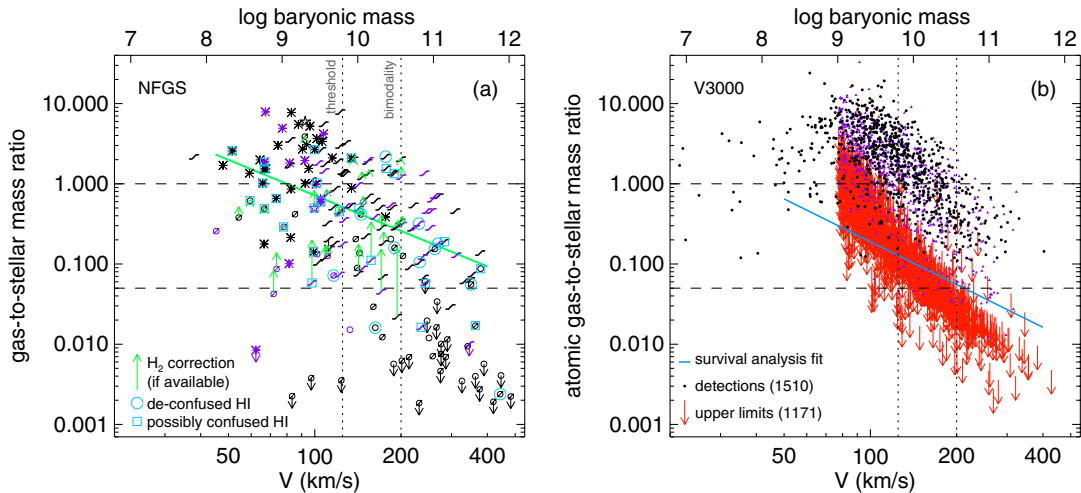
Figure 7. $M_{\rm gas}/M_*$ vs. internal velocity V for galaxies in (a) the NFGS (H I + H$_2$ where available) and (b) the V3000 sample limited at $M_r = -17.73$ (H I only). Horizontal and vertical lines repeated in both panels mark key mass and gas-richness scales for reference. Downward arrows mark upper limits in both samples; the dramatic difference in scatter between the two samples illustrates the importance of strong limits. The blue line in panel (b) indicates a survival analysis fit to the V3000 data, which attempts to take into account upper limits; this fit is unrealistic in lying below the fit to the NFGS data in panel (a) (green line) but nonetheless shows that the apparently tight trend seen for the V3000 detections is misleading (see Section 3 for further discussion). Galaxies without reliable direct V measurements are plotted using the V inferred from the baryonic M–V relation (NFGS galaxies) or M_r–V relation (V3000 galaxies) and colored purple. The baryonic mass conversion determined over the full mass range of the NFGS is shown on both top axes (see Figure 6 caption). *Further notes for panel (a):* Morphology symbols are as in Figure 1. Green upward arrows indicate molecular gas corrections where available. Blue circles mark galaxies with known companions in the GBT beam; for these galaxies we attempt separation of any confused flux in the profile using optical kinematic data. Blue boxes mark possibly confused literature data (Section 2.1.2). The green solid line is a fit minimizing residuals in $M_{\rm H I}/M_*$, excluding extremely gas-starved galaxies (those with $M_{\rm H I}/M_* < 0.01$ or an upper limit), which yields $\log M_{\rm H I}/M_* = 2.80 - 1.47 \log V$ with 0.58 dex scatter in $\log M_{\rm H I}/M_*$. Excluding galaxies below $M_{\rm H I}/M_* \sim 0.05$ reduces the scatter to 0.50 dex but yields an even shallower slope: $\log M_{\rm H I}/M_* = 2.40 - 1.24 \log V$.
(A color version of this figure is available in the online journal.)

outliers (circled in orange in Figure 6). We infer that most E/S0s are rotation supported below the threshold scale (and therefore treat their V measurements as unreliable unless they are unambiguously dynamically hot or have reliable gas-derived velocities). This population includes many blue-sequence E/S0s in low-density environments, consistent with a formation scenario involving increasingly gas-dominated mergers below the threshold scale, as expected from Figure 7 (and logically extending the wet/dry merger scenario used by Emsellem et al. 2007 to explain the fast/slow rotator dichotomy for E/S0s above the bimodality scale).

Late-type galaxies also deviate from the stellar M–V relation below the threshold scale, in the sense of *higher* V at a given mass. However, this deviation is diminished by the inclusion of $M_{\rm H I}$ to recover a tight "baryonic" Tully–Fisher relation (McGaugh et al. 2000). The onset of significant deviations is most easily seen by comparing the stellar M–V relation to the fit from the baryonic M–V relation, which is derived for all galaxies with $M_{\rm bary} > 10^{10} M_\odot$ in Figure 6(b) and shifted to the mean M_* for the late types among these galaxies in Figure 6(a). The gas mass correction becomes important below $V \sim 125$ km s^{-1}, exactly where gas-dominated galaxies become abundant (Figure 7). It is intriguing that even after we add $M_{\rm H I}$, the M–V relation remains slightly offset to higher V below $V \sim 125$ km s^{-1}. The remaining offset could reflect either a change in relative baryonic-to-dark matter concentration below the threshold scale or an additional undetected gas reservoir. Previous studies of the baryonic Tully–Fisher relation have argued that adding a multiple of the H I-derived gas mass yields the tightest M–V relation, implying the possibility of undetected gas in ionized, CO-dark molecular, or optically thick atomic form (Pfenniger & Revaz 2005; Begum et al. 2008).

The threshold and bimodality scales are associated with two physically significant transitions in galaxy gas content, seen most clearly in the NFGS (Figure 7(a)): below the threshold scale, gas-dominated galaxies with gas-to-stellar mass ratios $M_{\rm H I}/M_* > 1$ become noticeably more abundant, while above the bimodality scale, gas-starved galaxies with $M_{\rm H I}/M_* < 0.05$ start to predominate.[21] Molecular gas corrections are provided where CO data are available (green arrows) and do not significantly affect the trends; H$_2$ contributions generally become significant only when overall gas content is low. To a significant extent, bulgeless and bulge-dominated galaxies correspond to gas-dominated and gas-starved galaxies, respectively. However, S0–S0a galaxies are not always bulge-dominated (see Figure 1(b)), and they may have significant gas (as reported by many authors; e.g., Hawarden et al. 1981; Sage & Welch 2006), which complicates analysis by Hubble type.

Patterns of gas content are obscured by weak upper limits in the V3000 sample (Figure 7(b)), creating a misleadingly tight trend. To illustrate the extent of the problem, the blue line in Figure 7(b) shows a fit using survival analysis to include upper limits. Specifically, we make use of the Buckley–James estimator (discussed as most robust to non-Gaussian scatter by Isobe et al. 1986), as implemented in the ASURV package (Rev. 1.2; Lavalley et al. 1992). The survival analysis fit lies well below the detected data and in fact even below the conventional fit for the NFGS data in Figure 7(a). However, we stress that the survival analysis result should not be overinterpreted, because survival analysis assumes that the incidence of upper limits is uncorrelated with the underlying values, an assumption often treated as roughly valid for flux-limited surveys but clearly

---

[21] The choice of $M_{\rm H I}/M_* \lesssim 0.05$ as a transitional value is motivated by the fact that nearly all spiral-type systems are detected with $M_{\rm H I}/M_* > 0.05$; however, the preponderance of upper limits for E/S0s even down to $M_{\rm H I}/M_* \lesssim 0.002$ leaves open the possibility that typical $M_{\rm H I}/M_*$ values for gas-starved E/S0s may actually be much lower than 0.05.

violated once distance limits are imposed as in the volume-limited V3000 sample. In Section 4.4.1 we will use an updated calibration of the photometric gas fraction technique (K04) to show that the full V3000 $M_{\rm H\,I}/M_*$ distribution likely looks quite similar to that of the NFGS.

In fact, the *lack* of a tight relationship between $M_{\rm H\,I}/M_*$ and V for the NFGS may be the most important result seen in Figure 7. We stress that the extreme diversity of $M_{\rm H\,I}/M_*$ in the NFGS is *real*, reflecting its selection as a broadly representative sample of the galaxy population, whereas the seemingly tighter $M_{\rm H\,I}/M_*$ versus V relation for the V3000 sample is created by weak upper limits as just discussed. Moreover, other data sets that may have *seemed* to show a tight dependence of gas content on galaxy mass have also been inherently detection biased and/or selection biased (for example, as in the work of K04 and McGaugh 2005, both widely used to estimate gas mass from stellar mass, e.g., as in Stewart 2011). We also note that past studies have generally plotted $M_{\rm H\,I}/M_*$ versus M_*, in which case the usual $\gtrsim 0.2$ dex errors in M_* combined with the covariance between plot axes will spuriously enhance the impression of a correlation. Figure 7 shows gas-richness transitions using V as our preferred mass proxy, since it correlates tightly with baryonic mass and avoids covariance with $M_{\rm H\,I}/M_*$. With this choice, we do see *some* measurable trend in $M_{\rm H\,I}/M_*$ versus V, but the large scatter around the fit ($\gtrsim 0.5$ dex excluding quenched galaxies) implies little predictive power not already contained in the statement that gas-dominated galaxies start to appear in large numbers below the threshold scale. Furthermore, compared to gas-dominated galaxies, gas-starved galaxies appear less closely tied to their characteristic mass scale, with examples at all galaxy masses in spite of the potential bias against gas-poor dwarfs in the *B*-selected NFGS.

Previous work has suggested abrupt changes in ISM physics at the threshold scale (Dalcanton et al. 2004), so the question of whether gas-richness is changing sharply at $V \sim 125$ km s^{-1} in Figure 7 is of interest. The small number statistics of the NFGS do not allow us to establish whether the transition is sharp or continuous in that sample. The V3000 sample is larger, but also fails to confirm an abrupt transition, although a sharp transition could perhaps be hidden by its larger measurement uncertainties. Regardless, we will argue in Section 4 that galaxy mass (or its proxy V) is *not* the most fundamental variable underlying transitions in gas richness, and that the broad scatter in $M_{\rm H\,I}/M_*$ at low V implies additional physics.

4. GAS RICHNESS, LONG-TERM FSMGR, AND REFUELING REGIMES

We have argued that distinct transitions occur at the threshold and bimodality scales, coupling gas-richness changes with structural changes. Yet we have also seen considerable diversity in galaxy properties at any given mass. Here we demonstrate that U–NIR colors perform far better than galaxy masses in predicting gas-richness and morphology. We show that these colors can be understood as proxies for the long-term fractional stellar mass growth rate, FSMGR$_{\rm LT}$, averaged over the last Gyr. We further argue that the most natural interpretation of the tight $M_{\rm H\,I}/M_*$ versus FSMGR$_{\rm LT}$ relation involves routine fresh gas accretion, and we identify three distinct regimes in FSMGR$_{\rm LT}$, $M_{\rm H\,I}/M_*$, and morphology that we link to qualitatively different states of external gas accretion and internal gas processing ("refueling regimes"). Finally, we examine the mass dependence of the refueling regimes to show how they give rise to the threshold and bimodality scales.

4.1. The Tight Relation of $M_{\rm H\,I}/M_*$ versus U–NIR Color

U–NIR colors define a surprisingly tight correlation with $M_{\rm H\,I}/M_*$, providing the basis for the photometric gas fraction technique of K04. In contrast to the $\sigma \sim 0.58$ dex scatter in the $M_{\rm H\,I}/M_*$ versus V relation (Figure 7(a)), we measure 0.36 dex scatter in the $M_{\rm H\,I}/M_*$ versus $(u - J)^m$ color relation (Figure 8(a)), using the same subset of NFGS galaxies (i.e., excluding extremely gas-starved systems with $M_{\rm H\,I}/M_* < 0.01$ or upper limits). We obtain 0.30 dex scatter in $M_{\rm H\,I}/M_*$ versus $(u - J)^m$ when excluding gas-starved systems with $M_{\rm H\,I}/M_* < 0.05$, as compared to the 0.50 dex scatter measured for the same galaxies in $M_{\rm H\,I}/M_*$ versus V. Moreover, since exclusions based on gas content are impractical from the point of view of predicting gas content, it is especially interesting that gas-starved galaxies are *tightly confined* in Figure 8(a) to colors redder than $(u - J)^m = 3.7$. U–NIR color alone does not separate these gas-starved, spheroid-dominated galaxies from the reddest bulged disks (which have non-negligible gas and continue the $M_{\rm H\,I}/M_*$ versus $(u - J)^m$ correlation). Galaxies bluer than $(u - J)^m = 3.7$ display 0.34 dex scatter around the fit shown, excluding the one outlier, whose nature is uncertain.[22] As the typical stellar mass uncertainty for the NFGS is 0.15 dex, and systematic errors in stellar mass estimation are likely to be significantly larger (see Kannappan & Gawiser 2007), measurement uncertainties likely contribute much of the observed scatter in Figure 8(a), implying an impressively tight underlying correlation.

The $M_{\rm H\,I}/M_*$ versus $(u - J)^m$ relation given in Figure 8(a) supersedes that of K04, with higher quality data (reprocessed SDSS and 2MASS imaging; carefully vetted, largely new H I measurements), superior stellar mass estimation (from SED modeling rather than the $g - r$ versus M_*/L_K calibration of Bell et al. 2003), and a more representative galaxy sample spanning the natural diversity of galaxy gas-richness (as opposed to the inhomogeneous literature compilation used by K04). Given the far greater *intrinsic* diversity of the NFGS compared to prior samples used to calibrate the photometric gas fraction technique (K04; Zhang et al. 2009; Catinella et al. 2010; Li et al. 2012), it is remarkable that the scatter in our U–NIR relation is the same as has been obtained by these authors only by combining multiple parameters (e.g., optical color, surface brightness, stellar mass, and/or color gradient). We infer that U–NIR colors capture the physics of galaxy gas richness in an essential way, to be discussed in Section 4.2. However, we also note that internal extinction is responsible for some fortuitous straightening and tightening of the $(u - J)^m$ relation: if replotted using the extinction-corrected $(u - J)^e$, Figure 8 appears more similar to the bowed NUV$-r$ relation (e.g., as reported by Catinella et al. 2010). Moreover, our reprocessed $u - r$ colors (unlike SDSS catalog $u - r$ colors) are comparable to U–NIR colors in predictive power (K. D. Eckert et al., in preparation).

4.2. U–NIR Color as a Long-term FSMGR Metric

As shown in Figure 8(b), the primary physics underlying the $(u - J)^m$–$M_{\rm H\,I}/M_*$ correlation is another tight correlation,

---

[22] The plot location of the outlier in Figure 8(a), UGC 4879, is either spurious or intriguing, as it is both (1) a post-starburst galaxy, with strong Balmer absorption and no detectable Hα emission; and (2) very nearby, with individually resolved star clusters and clumpy, irregular structure, making our photometry highly unreliable (Section 2.1.1).
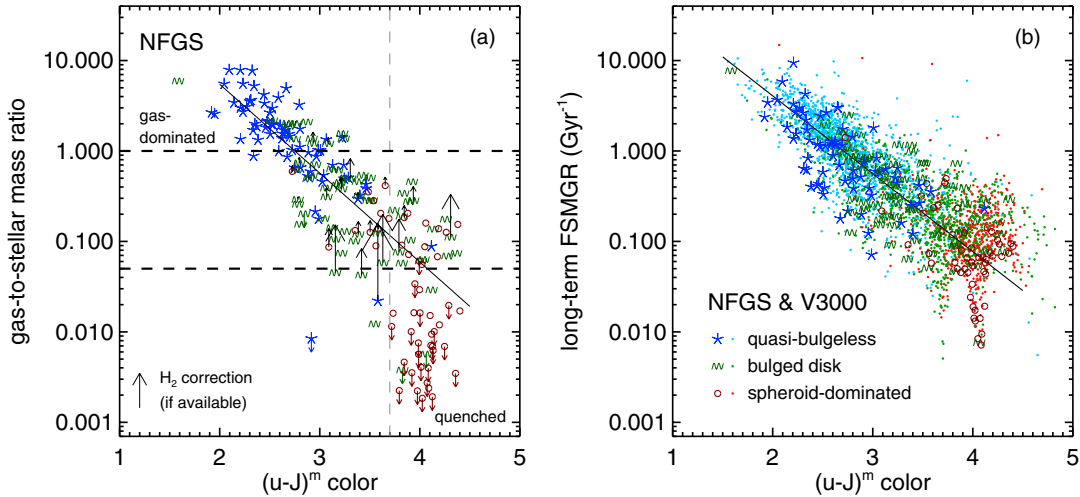
Figure 8. Gas-richness and long-term fractional stellar mass growth rate FSMGR$_{LT}$ in relation to U–NIR color, with symbols indicating μ_Δ morphology class as defined in Figure 1(b). (a) M_{HI}/M_* vs. $(u - J)^m$ color for the NFGS. The solid line is a fit minimizing residuals in M_{HI}/M_* for all galaxies bluer than $(u - J)^m = 3.7$ (excluding the outlier, see footnote 22), which yields log $M_{HI}/M_* = 2.70 - 0.98(u - J)^m$ with 0.34 dex scatter. If available, molecular gas corrections are shown with black arrows but are not used in the fit. (b) Mapping of $(u - J)^m$ color to FSMGR$_{LT}$, determined by fitting to a suite of two-component old+young stellar population models as described in Section 4.2. Small dots show V3000 sample galaxies with $M_r < -17.73$. We measure 0.30 dex rms scatter around the V3000 sample fit (black line: log FSMGR$_{LT} = 2.33 - 0.861(u - J)^m$ for galaxies bluer than $(u - J)^m = 3.7$), which is comparable to the scatter in panel (a).

(A color version of this figure is available in the online journal.)
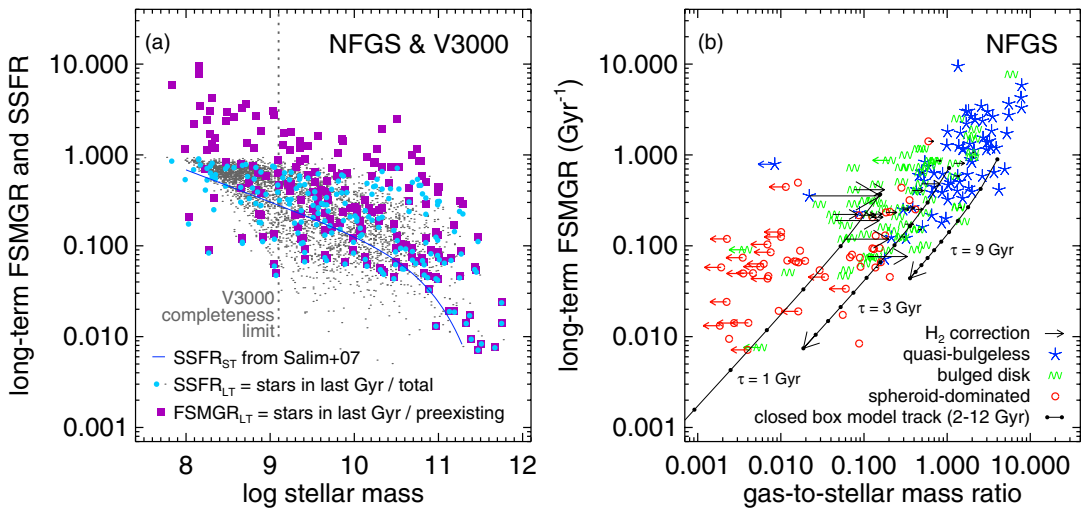
Figure 9. FSMGR$_{LT}$ as a function of stellar mass and M_{HI}/M_*. (a) Comparison of FSMGR$_{LT}$ and SSFR$_{LT}$ derived from stellar population modeling of NFGS galaxies (large colored symbols) reveals the essential difference between these quantities: FSMGR divides by preexisting rather than by total mass, so it does not asymptote to one over the unit of time at high growth rates. Small background dots represent SSFR$_{LT}$ values for the V3000 sample (down to $M_r = -17$, hence incomplete below the M_* limit shown; Section 2.2). Comparison of the V3000 and NFGS distributions confirms that the NFGS is broadly representative of the general galaxy population, albeit with overrepresentation of high-SSFR galaxies consistent with its parent survey's B-band selection. Comparison of the V3000 distribution with the short-term SSFR trend (blue line) provided by S07 reveals an overall shift toward higher SSFRs in our long-term measurements. While some of this effect may reflect the timescale difference, we suspect that photometry differences are more important: as discussed in Section 2.1.1, our photometry yields significantly bluer $u - r$ colors than the SDSS DR7 catalog photometry used by S07. (b) FSMGR$_{LT}$ and M_{HI}/M_* define a nearly one-to-one relation on Gyr timescales (note the identical axis ranges). Closed box model tracks (whose arrows point in the direction of greater age) are inconsistent with the data except for the first few time steps, representing galaxies born ~2–5 Gyr ago. We interpret these results in terms of cosmic accretion in Sections 4.3 and 4.4. We identify three refueling regimes: (1) a gas-dominated, stellar mass doubling (FSMGR > 1) regime; (2) a transitional regime with growth rates and gas fractions at tens of percentage levels; and (3) a gas-starved, minimal growth regime considered quenched. Symbols indicate μ_Δ classes, which approximately map to these regimes, with interesting complexity in the transition range (see Section 4.4).

(A color version of this figure is available in the online journal.)

between $(u - J)^m$ and FSMGR$_{LT}$ where:

$$\text{FSMGR}_{LT} = \frac{\text{mass}_{\text{formed in last Gyr}}}{1\,\text{Gyr} \times (\text{mass}_{\text{preexisting}})}. \qquad (4)$$

We measure FSMGR$_{LT}$ as part of the same stellar population modeling used to determine stellar masses (Section 2.1.1). Our model grid is designed to sample FSMGR$_{LT}$ uniformly in the logarithm, with 13 values from 10^{-3}, $10^{-2.65}$, $10^{-2.3}$,..., up

to $10^{1.2}$. We estimate both the likelihood-weighted mean and the likelihood-weighted median FSMGR$_{LT}$ for each galaxy, but since they are very similar, we plot the means for visual clarity (the medians are discretized by construction).

The definition of FSMGR$_{LT}$ may seem superficially similar to that of a specific star formation rate (star formation rate normalized to current stellar mass), e.g., as traced by EW(Hα) over short timescales. However, FSMGR$_{LT}$ is not equivalent to a

long-term SSFR, because the newly formed stellar mass appears only in the numerator. In contrast, conventional definitions of SSFR (e.g., as in the work of S07) include new stellar mass in both the numerator and the denominator, so that at high growth rates the SSFR cannot exceed one over the unit of time in which the SFR is measured (see Figure 9(a)). Thus, SSFRs offer limited insight into star formation in high fractional growth regimes.

Plotting $FSMGR_{LT}$ directly against M_{HI}/M_*, we find a remarkably linear relationship for star-forming galaxies (Figure 9(b)). It is particularly striking that in per Gyr units, the newly formed-to-preexisting stellar mass ratios for quasi-bulgeless and bulged disk galaxies are not merely *proportional* to their gas-to-stellar mass ratios, but instead are *almost the same.* The numerical coincidence of scales on the $FSMGR_{LT}$ and M_{HI}/M_* axes has profound implications to be discussed in Section 4.3, so it is worth noting that our estimates of $FSMGR_{LT}$ are higher than would be expected from previous work. Specifically, if we convert our FSMGRs to SSFRs (dots in Figure 9(a)), we find that both the V3000 sample and the NFGS lie above the fit line for short-term SSFRs from S07. A small amount of this difference may be due to the short-term versus long-term measurement (see Salim et al. 2009), and the excess of scatter for the NFGS may certainly reflect the blue selection of its parent survey (Jansen et al. 2000b), but the majority of the effect is probably due to differences in photometry: as discussed in Section 2.1.1, our reprocessed SDSS magnitudes yield significantly bluer colors than the SDSS DR7 catalog photometry used by S07.

4.3. Interpreting the M_{HI}/M_* versus $FSMGR_{LT}$ Relation

Since gas fuels star formation, it may seem self-evident that $FSMGR_{LT}$ should correlate with M_{HI}/M_*. Indeed, Zhang et al. (2009) have argued that the Kennicutt–Schmidt relation can be used to explain the correlation of another long-term star formation tracer, $g - r$ color, with M_{HI}/M_*. Motivated by the Kennicutt–Schmidt relation, they add i-band surface brightness to $g - r$ color to obtain a correlation with M_{HI}/M_* with 0.31 dex scatter, albeit with a less diverse/representative sample than we have presented (following K04, they analyze galaxies with H I detections in HyperLEDA). Despite the appeal of their straightforward interpretation, there are two reasons to rethink the underpinnings of the photometric gas fraction technique.

First, most astronomers agree that stars form in molecular gas (e.g., Krumholz et al. 2011). Yet U–NIR colors correlate only with atomic gas or the combination of atomic+molecular gas—a plot of U–NIR colors versus M_{H_2}/M_* is a scatter plot (red points in Figure 10). A typical plot of the Kennicutt–Schmidt relation would show that the Hα-derived star formation rate has a direct correlation with the mass in H_2, its immediate precursor, where both are typically divided by surface areas to yield surface densities (e.g., Bigiel et al. 2008; Schruba et al. 2011). The timescales involved in the Kennicutt–Schmidt relation are measured in tens of Myr, so long-lasting U-band flux is not an ideal real-time tracer of star formation and molecular gas consumption. In contrast, U–NIR color tracks $FSMGR_{LT}$ over timescales long enough to register whether molecular gas is resupplied from a larger reservoir. Because H I can resupply H_2 and makes up most of the gas in a typical galaxy (H_2-rich galaxies are relatively less common and also typically gas-poor; Figures 7(a), 8(a), and 10), H I measurements generally trace a galaxy's potential for long-term molecular gas consumption better than H_2 measurements, which reflect only current H_2. For the few galaxies in Figure 8(a) with large H_2

corrections (green arrows), the H_2 represents a large fraction of the total gas reservoir and thus helps tighten the U–NIR versus M_{gas}/M_* relation. Of course, short-term processes that affect H_2 and EW(Hα) also affect U–NIR colors—we see that EW(Hα) varies with $(u - J)^m$ in Figure 10(a)—but the scatter in the plot of M_{HI}/M_* versus EW(Hα) is >20% higher than in the plot of M_{HI}/M_* versus $(u - J)^m$ (Figure 10(b) versus Figure 10(a)). The long timescale of U–NIR colors would seem optimal for predicting M_{HI}/M_*, implying that the underlying physics is distinct from the short timescale physics driving the Kennicutt–Schmidt relation.

Moreover, the long U–NIR timescale suggests a second level of reinterpretation. We have shown that U–NIR colors reflect $FSMGR_{LT}$ past-averaged over a Gyr (Section 4.2). Why such long-term past-averaged star formation should correlate tightly with *present* gas richness is not obvious in a "gas reservoir causes star formation" picture. One might suppose that the correlation could result from a well-behaved time lag between M_{HI}/M_* and $FSMGR_{LT}$ in a closed box scenario, but again we note the surprising fact that these quantities are not just proportional, but *nearly the same* when star formation is integrated over the last Gyr. This fact, along with the modest scatter for non-gas-starved galaxies in Figure 9(b), rules out any reasonable closed box model. To illustrate the difficulty, we show three model tracks in Figure 9(b), with gas depletion times of 1, 3, and 9 Gyr. The tracks obey pure closed box evolution:

$$M_{gas}/M_* = \frac{e^{-t/\tau}}{1 - e^{-t/\tau}}, \qquad (5)$$

$$FSMGR_{LT} = \frac{e^{-(t-1)/\tau} - e^{-t/\tau}}{1 - e^{-(t-1)/\tau}}, \qquad (6)$$

where τ is measured in Gyr. Intersection with the data requires an implausibly young box (just a few Gyr), which should ideally also have short gas depletion time.

The most natural way out of this cause-effect conundrum is to suppose that most galaxies are routinely refueled, both in the sense of external gas accretion and in the sense of internal gas transport and H I-to-H_2 conversion. In this view, the coincidence of axes in Figure 9(b) implies that the entire cold gas reservoir of an unquenched galaxy is routinely turned into stars and fully replenished over the time span of a Gyr, within a factor of a few. It follows that Gyr timescales must be longer than the typical time intervals between any discrete processes necessary to maintain refueling and star formation, such as gas accretion events, development of internal instabilities, and/or interactions with companions. Thus, the fundamental physics underlying the M_{HI}/M_* and $FSMGR_{LT}$ relation involves gas refueling on roughly Gyr timescales.

4.4. Refueling Regimes

From a refueling perspective, three regimes emerge naturally from Figure 9(b), reflecting coordinated shifts in gas richness, growth rate, and morphology (as parameterized by μ_Δ class in Figures 8 and 9). The *accretion-dominated* regime of gas-dominated quasi-bulgeless disks is characterized by extremely rapid growth ($FSMGR_{LT} \sim 1$ implies stellar mass doubling on Gyr timescales) and ultra-blue colors. The *processing-dominated* regime of "normal" bulged disks is mostly characterized by moderate growth and gas content at tens of percentage levels, but these transitional systems show greater diversity in color and gas content than quasi-bulgeless or spheroid-dominated systems (Figure 11). We will argue in
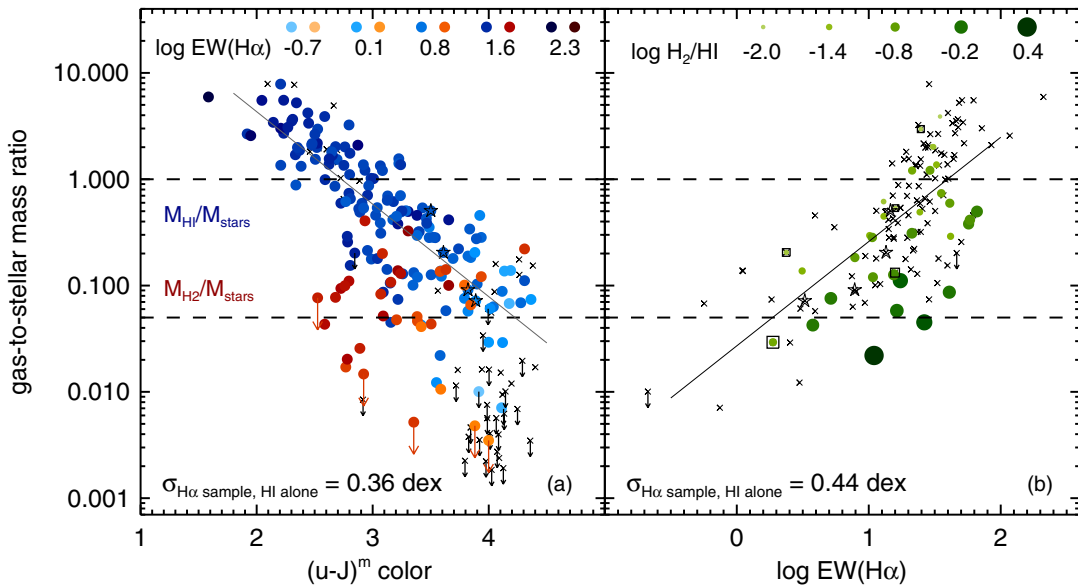
Figure 10. Relationship of gas-to-stellar mass ratios to long-term and short-term $\langle SSFR \rangle$, as parameterized by U–NIR color and EW(Hα), respectively, for the NFGS. (a) M_{HI}/M_* (blue) and M_{H2}/M_* (red) vs. $(u - J)^m$ color as in Figure 8(a), with points coded by EW(Hα) as shown in the legend ($\times$ symbols mark galaxies either lacking Hα data or undetected in Hα). Downward arrows indicate upper limits. Stars mark AGNs as classified by Jansen et al. (2000a). (b) M_{HI}/M_* vs. EW(Hα), with points coded by H_2/HI mass ratio as shown in the legend. Additional symbols are as in panel (a), except now $\times$ symbols mark galaxies lacking H$_2$ data and boxed points denote H$_2$ upper limits. The scatter in panel (b) is notably higher than in panel (a), relative to fits restricted to Hα-detected galaxies in both panels.

(A color version of this figure is available in the online journal.)
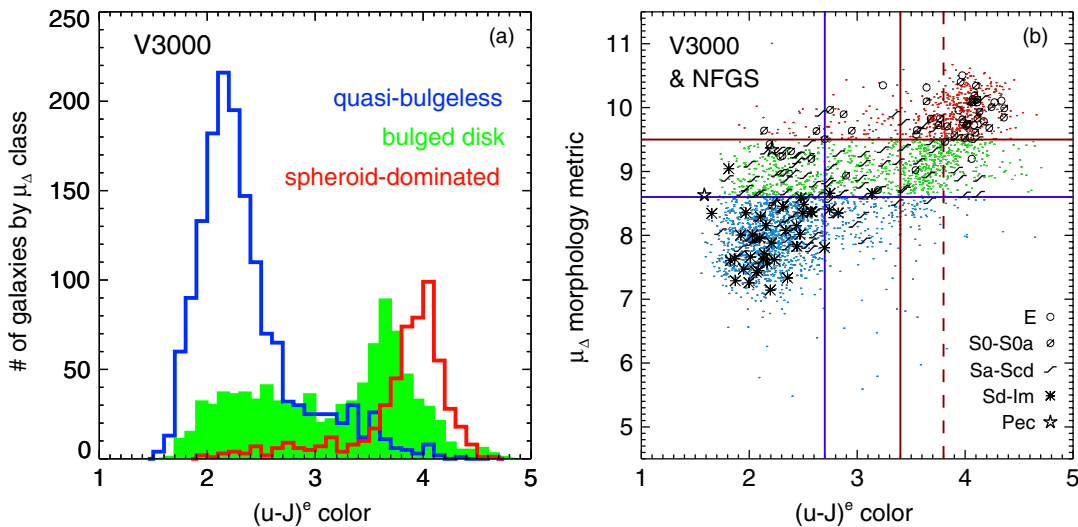
Figure 11. Galaxy morphology in relation to de-extincted $(u - J)^e$ color, using μ_Δ classes for the V3000 sample ($M_r < -17.73$) and traditional morphological types for the NFGS. Horizontal lines in panel (b) mark the divisions used to define the three μ_Δ classes (see Figure 1), while vertical lines mark shifts in their relative dominance as seen in panel (a). Ultra-blue fast-growing quasi-bulgeless galaxies and red-and-dead spheroid-dominated galaxies occupy distinct loci. Bulged disk galaxies are transitional, displaying a broad range of colors, but also show a clear peak starting at $(u - J)^e \sim 3.4$, just shy of the quenched spheroid regime. Visual inspection of galaxies in this peak reveals residually star-forming S0 or dying spiral galaxies.

(A color version of this figure is available in the online journal.)

Section 4.4.3 that this regime may also be considered to include blue spheroid-dominated galaxies, to the extent that they are likely to regrow disks rather than quench. Finally, the *quenched* regime of red-and-dead spheroid-dominated galaxies is characterized by gas poverty ($M_{HI}/M_* \lesssim 0.05$) and slow growth (FSMGR$_{LT} \lesssim 0.1$), although the exact definition of this regime is debatable, given the existence of a distinct population of *nearly* quenched bulged-disk systems with $(u - J)^e = 3.4$–3.8 as seen in Figure 11.

Below we examine the significance of these regimes in the context of a broader picture of galaxy evolution. We first relate regime transitions to the threshold and bimodality scales

reviewed in Section 3, with attention to the complicating factor of environment, and then go on to discuss implications of the refueling regime picture for galaxies typical of each regime.

4.4.1. Regime Transitions and Galaxy and Halo Mass Scales

The existence of red disk and blue spheroid crossover systems in Figure 11 points to the complexity of refueling and quenching, likely reflecting the influence of large-scale environment as well as local galaxy interactions and mergers. Environmental analysis of the V3000 sample and its parent survey will be presented elsewhere (A. J. Moffett et al., in preparation; K. D. Eckert et al., in preparation; S. J. Kannappan et al., in preparation), but

for the present discussion we note that these studies present a general picture in which galaxies that are central (most massive) in their dark matter halos follow the simplest trajectories from accretion-dominated to quenched, as judged by U–NIR colors, while satellite galaxies display greater diversity, including some of the most extreme crossover states. This picture reinforces that of Peng et al. (2012), who argue that central galaxies experience essentially zero environmentally driven evolution, quenching solely as a function of galaxy mass, while satellites are responsible for all signatures of quenching that increase with group halo mass. Thus, central/satellite differences offer a way to reconcile the scattered dependence of gas-richness on galaxy mass with the existence of clear gas-richness transitions at the threshold and bimodality scales, below and above which, respectively, galaxies typical of the accretion-dominated and quenched regimes become abundant (as seen in Section 3 and further confirmed for the V3000 sample below).

If we assume that observed transitions in gas-richness, morphology, and dynamics at the threshold and bimodality scales reflect the en masse transformation of central galaxies, then we can link these scales to equivalent halo mass scales. At the threshold scale, the central-galaxy M_*-to-M_{halo} calibration of Behroozi et al. (2013) indicates that $M_* \sim 10^{9.7} \ M_\odot$ corresponds to $M_{halo} \sim 10^{11.5} \ M_\odot$. Equivalently, the threshold velocity of $\sim$125 km s^{-1} matches a halo virial velocity of $V_{vir} \sim 100$ km s^{-1} if $V_{galaxy}/V_{vir} \sim 1.3$, as reported by Reyes et al. (2012). At the bimodality scale, the same logic implies halo parameters of $M_{halo} \sim 10^{12.1} \ M_\odot$ and $V_{vir} \sim 160$ km s^{-1}.

These two halo mass scales are potentially important in relation to cosmic accretion. First, observational analysis suggests that *above* a halo mass of $\sim 10^{12.1} \ M_\odot$, central galaxy M_* rises much more slowly with growing halo mass (Leauthaud et al. 2012), implying that the primary mode of central galaxy growth that operates at lower halo mass is being valved off above $M_{halo} \sim 10^{12.1} \ M_\odot$ (corresponding to the bimodality scale). Second, several theoretical prescriptions suggest that somewhere in the range $M_{halo} = 10^{11}$–$10^{12} \ M_\odot$ (likely corresponding to the threshold scale), halo gas cooling becomes much more efficient, such that $\gtrsim$50% of baryons accreted onto the halo over the age of the universe cool within the same time (Lu et al. 2011). In the specific case of the "cold-mode" accretion picture (Birnboim & Dekel 2003; Keres et al. 2005), wherein slow hot-mode accretion replaces rapid cold-mode accretion as shock heating becomes more effective with increasing halo mass, calculations by Dekel & Birnboim (2006, see their Figures 2 and 3) show that at $z = 0$, the shock-heating transition occurs in the *inner* halo at $0.1\times$ the virial radius for halos with $V_{vir} \gtrsim 100$ km s^{-1} (the threshold scale for centrals), while the transition expands to the outer halo past the virial radius for halos with $V_{vir} \gtrsim 170$ km s^{-1} (the bimodality scale for centrals). Recent work using the moving-mesh AREPO code questions the details of this picture, as about half of simulated cold-mode accretion may reflect numerical artifacts (Nelson et al. 2013), yet overall accretion rates onto halos are actually higher using AREPO, due to faster cooling of the hot mode, and the general halo mass dependence of cooling remains. Furthermore, we note that the onset of a "rapid" accretion mode when the cooling radius exceeds the halo virial radius is a common feature of many semi-analytic cooling prescriptions, as reviewed by Lu et al. (2011), most of which do not involve a cold-mode/hot-mode distinction per se.

In this context, it is interesting to revisit the possibility of a *sharp* transition at the threshold scale as proposed by Dalcanton

et al. (2004), which might constrain theoretical models of accretion. To construct a statistically robust sample to test this possibility, we first estimate baryonic masses for the full V3000 sample down to $M_r = -17$. We adopt the photometric gas fraction estimator presented in Figure 8(a) for galaxies with $(u - J)^m < 3.7$:

$$\log M_{HI}/M_* = 2.70 - 0.98(u - J)^m \qquad (7)$$

with 0.34 dex scatter. We assign gas masses using Monte Carlo methods to produce realistic variations matching this 0.34 dex scatter in M_{HI}/M_*, while not allowing gas masses higher than the measured upper limits. For galaxies redder than $(u - J)^m = 3.7$, we assign gas fractions randomly in the logarithmic interval from $M_{HI}/M_* = 0.001$ to the limit value or 0.5, whichever is smaller. Finally, we sub-select a baryonic mass-limited sample from the V3000 data set with $M_{bary} > 10^{9.3} \ M_\odot$ (the expected completeness limit; see Section 2.2). The M_{HI}/M_* versus V distribution for this sample is plotted in Figure 12(a). Note that the offset in V between detections and limit replacements is due to the fact that most detections can scatter to low or high V, whereas limits (and some detections, e.g., those with $i < 50$ deg) must be plotted with an inferred V from the all-galaxy M_r–V relation, which tends to overestimate V for gas-poor galaxies (Figure 6).

Based on this analysis, Figure 12(a) shows no obviously sudden onset of gas-richness for the V3000 sample. We do see that gas-dominated galaxies become the majority population roughly below the threshold scale (histograms at the top of Figure 12(a)), and that the V3000 sample shows the same large, strongly mass-dependent scatter in M_{HI}/M_* that we saw for the NFGS in Figure 7, lending credence to the NFGS results. Gas-starved dwarfs are now represented (based on $(u - J)^m$) but drop sharply in relative frequency as gas-dominated galaxies become more common. Furthermore, the gas-starved dwarf population resides predominantly in the highest-density environments seen in Figure 4, such as the Coma Cluster, implying environmental quenching. By contrast, the majority of dwarf galaxies are isolated and gas-rich.

4.4.2. The Accretion-dominated Regime

For the quasi-bulgeless, gas-dominated disks typical of the accretion regime, fresh gas is accreted as fast as or faster than it can be consumed, based on Figure 9(b). Most quasi-bulgeless disks scatter around $FSMGR_{LT} \sim 1 \ Gyr^{-1}$, suggesting that they are capable of doubling their stellar masses each Gyr. Thus, *typical gas-dominated Sd–Im galaxies are growing exponentially*, at least in the "high-mass dwarf" regime we explore (Bouché et al. 2010 note the possibility of an accretion "floor" that could prevent effective gas cooling for lower-mass galaxies). This conclusion is consistent with that of Moster et al. (2013), who infer from a multi-epoch halo abundance matching analysis that today's low-mass galaxies are still increasing in star formation rate (where these authors' definition of low mass roughly equates to below the threshold scale).

The standard counterargument supposes that dwarf galaxies have intrinsically bursty star formation and therefore experience off states that ensure low time-averaged SSFR despite high short-term SSFR (e.g., Feulner et al. 2005). However, we have measured high growth rates averaged over the last Gyr. Moreover, systematic searches for non-star-forming dwarf galaxies have shown them to be exceedingly rare in field environments
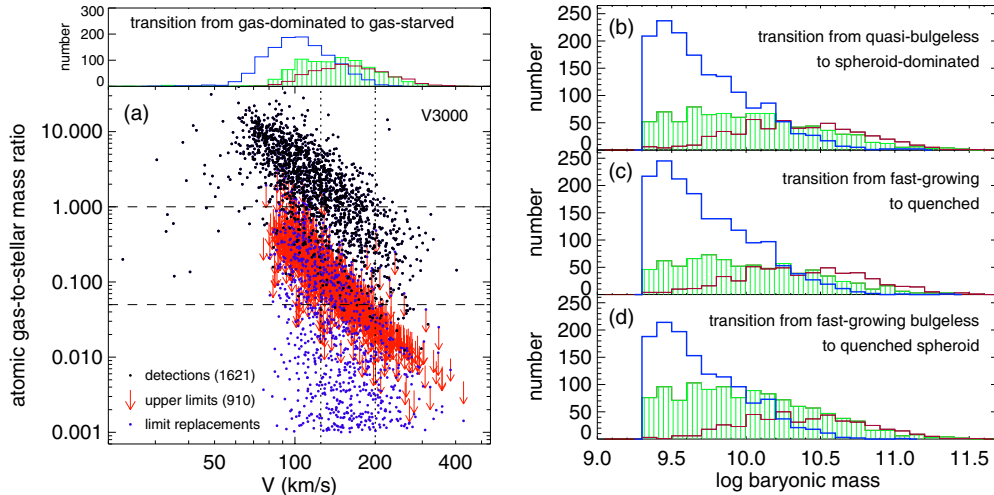
Figure 12. (a) $M_{\mathrm{H\,I}}/M_*$ vs. V for the V3000 sample, using the photometric gas fraction technique to replace upper limits with likely values based on $(u - J)^m$ color (see Section 4.4.1 for details). We now draw from the full V3000 sample down to $M_r = -17$ to identify galaxies with measured or estimated $M_{\mathrm{bary}} > 10^{9.3}\ M_\odot$, so the absence of quenched galaxies at low M_{bary} is plausibly correct (see Section 4.4.2 for further discussion). The offset in V between detections and limits is not significant but reflects the use of the all-galaxy M_r–V relation to provide V for limits (Section 2.2), which suppresses natural scatter. Vertical lines mark the threshold and bimodality scales, and horizontal lines divide the gas-dominated, intermediate-gas, and gas-starved regimes. Histograms of these regimes (blue, green, and red, respectively) are shown at the top of the panel, illustrating their relationship to the threshold and bimodality scales. (b)–(d) Mass distributions of galaxies in different color and morphology regimes for the baryonic mass limited sample shown in panel (a). We consider three ways of identifying the transitional regime (green histogram) with reference to Figure 11. In panel (b), transitional galaxies are those in the bulged disk μ_Δ class. In panel (c), transitional galaxies are those whose colors fall in the range $(u - J)^e < 2.7$–3.8, which is broadly inclusive of residually star-forming galaxies at the red end. In panel (d), transitional galaxies are all those that do not occupy the regions of $(u - J)^e$ vs. μ_Δ parameter space dominated by blue quasi-bulgeless systems ($(u - J)^e < 2.7$, $\mu_\Delta < 8.6$) or quenched spheroids ($(u - J)^e > 3.4$, $\mu_\Delta > 9.5$). Only by this hybrid definition does the transitional population become "typical" (in the sense of "more common than either other population considered separately") within the range between the threshold and bimodality scales.

(A color version of this figure is available in the online journal.)

(Lee et al. 2011; see also Lee et al. 2009) and, when found, to be associated with proximity to massive hosts (Geha et al. 2012). In the volume-limited V3000 sample, the sharply dropping relative frequency of gas-starved galaxies with decreasing galaxy mass in Figure 12 is likewise consistent with few (or brief) truly off states, although we remind the reader that this sample suffers from residual bias against low surface brightness dwarfs, which might in principle include a high mass-to-light ratio population (Section 2.2). Nonetheless, from the evidence in hand it is reasonable to conclude that most low-mass galaxies achieve high FSMGR$_{\mathrm{LT}}$ through sustained growth.

A related concern is the effect of outflows on dwarfs. However, the early idea that supernova feedback in dwarfs should expel their gas and turn them off (Dekel & Silk 1986) appears most relevant to galaxies much less massive than we consider, with $V \sim 30$ km s^{-1} (Mac Low & Ferrara 1999). Powerful outflows are indeed expected—the data of Martin et al. (2012) reveal a significant increase in the frequency of strong outflows for $z = 0.4$–1.4 galaxies with short-term SSFRs $\gtrsim 0.8$ Gyr^{-1}—but they are likely to regulate rather than terminate star formation (see the comparison of outflow scenarios in Davé et al. 2013). The cosmological simulations of Brooks et al. (2007) also provide another perspective, suggesting that even significant outflows are less important than low star formation efficiency in setting the gas and metal content of low-mass galaxies. Of course, "low" star formation efficiency in systems experiencing cosmic accretion may not imply low SSFRs in absolute terms, but simply star formation that cannot keep up with the inflow rate.

As noted by Khochfar & Silk (2011) in the course of interpreting high-redshift observations, galaxies with sustained high SSFRs may pose a challenge for current models of galaxy evolution. For example, the simulation-motivated analytic model of

Davé et al. (2012), which assumes an equilibrium between mass inflow, mass outflow, and star formation, would predict SSFRs reaching only ~ 0.2–0.3 Gyr^{-1} for isolated $z = 0$ galaxies near the threshold scale (in rough agreement with the simulations of van de Voort et al. 2011, in which feedback prevents accretion from reaching the ISM for such galaxies). In this context, it is interesting to consider the possibility of excess accretion, leading to non-equilibrium "puddling" of ionized gas, contrary to the assumptions of Davé et al. (2012). While we have argued that *cold* H I+H$_2$ gas cycles through galaxies on Gyr timescales, nothing in Figure 9 requires that ionized gas arrive at the same rate. In fact, analyses of the baryonic Tully–Fisher relation suggest that dwarf galaxies may contain three to four times larger gas reservoirs than their H I-derived gas masses imply (Pfenniger & Revaz 2005; Begum et al. 2008). Our own baryonic M–V relation in Figure 6 may be "missing" such a multiplier, which would straighten it out below $V \sim 125$ km s^{-1}.[23]

Any such excess gas would presumably end up being processed intermittently in merger-driven bursts (distinct from internally driven bursts as considered above), likely producing phenomena such as blue compact dwarfs (BCDs). BCDs have previously been linked to gas-rich dwarf–dwarf mergers (e.g., Pustilnik et al. 2001; Bekki 2008). If accretion rates remain high after such events, the remnants may enjoy rapid disk regrowth. For example, the BCD NGC 7077 (shown in Figure 7 at $M_{\mathrm{H\,I}}/M_* \sim 0.4$ and $V \sim 60$ km s^{-1} and classed as an S0a in the NFGS) reveals a combination of color gradients, molecular and atomic gas content, and *GALEX*-detected extended UV disk structure that together suggest that this galaxy is a post-merger

---

[23] Another interesting set of results in the literature centers on the possibility of substantial CO-dark molecular gas in dwarf galaxies (e.g., Madden et al. 1997). If such undetected H$_2$ gas were comparable in mass to the H I, it might explain some of the scatter in $M_{\mathrm{H\,I}}/M_*$ versus FSMGR$_{\mathrm{LT}}$.

system just starting to rebuild its disk (Moffett et al. 2012; S13). If such a galaxy enters a reduced accretion regime post-merger, it may give rise to an Sa–Sc spiral, while if it stays in a high accretion regime, it may soon revert to Sd–Im morphology. Consistent with this picture, kinematic signatures of past mergers are observed in the stellar components of even very late-type dwarf disks (e.g., counterrotating stars and/or thick disks; Kannappan & Fabricant 2001; Yoachim & Dalcanton 2005; Leaman et al. 2009, 2012).

The reader might reasonably object to the notion of exponentially growing Sd–Im galaxies based on the implausibility of efficient gas processing in such systems (although the rate of *molecular* gas conversion to stars in such galaxies may actually be higher than in spirals, e.g., Gardan et al. 2007; Pelupessy & Papadopoulos 2009). However, we stress that regardless of any deficiency in gas transport mechanisms, the fact that $FSMGR_{LT}$ values remain high in the accretion-dominated regime implies that accretion-dominated systems do not have to form stars *efficiently* in order to form them *rapidly*: the rate of gas influx is apparently sufficient to overwhelm any inefficiency in consumption. Moreover, it is not obvious that the conventional definition of star formation efficiency, i.e., the inverse of the timescale for the current rate of star formation to consume the current reservoir of gas, makes sense for accretion-dominated galaxies. Huang et al. (2012) report as a paradox the fact that the most gas-rich galaxies in ALFALFA have both the highest SSFRs and the lowest star formation efficiencies, and they attribute this paradox to a bottleneck in processing the gas. We would propose that the paradox arises from the fact that the English words "low efficiency" connote galaxies lazily consuming gas: if instead the gas is pouring in faster than even the highest-SSFR galaxies can possibly consume it, such galaxies might be better termed "overwhelmed" than "inefficient."

4.4.3. The Processing-dominated Regime

For galaxies in the processing-dominated regime, gas is still consumed roughly as fast as it is accreted (Figure 9(b), in agreement with Fraternali & Tomassetti 2012). For centrals whose halos are experiencing reduced cosmic accretion, the transition to a processing-dominated state may be self-reinforcing. Slowed dilution of the ISM with fresh gas and/or reduced metal loss in outflows may lead to more efficient H_2 formation on dust grains (Krumholz & Dekel 2012). This process may in turn increase consumption efficiency for the diminished infalling gas and accelerate the galaxy's evolution to a processing-dominated state (thus decelerating growth). In addition, mild quenching may encourage more prominent stellar bulges and more concentrated disks that further promote higher gas densities and more efficient star formation (e.g., Blitz & Rosolowsky 2006).

Notably, galaxies in the processing-dominated regime show deviations in M_{HI}/M_* that seem to correlate with high H_2/HI, based on the incomplete H_2 data available (Figure 9). Our previous analysis of NFGS galaxies has revealed bursty, correlated variations in central and outer disk colors and H_2/HI ratios, particularly for bulged disks (S13). These variations seem to reflect externally triggered gas inflow events and central star formation enhancements, with corresponding lulls in outer-disk growth (Kannappan et al. 2004; S13). The most extreme events lead to the formation of blue-sequence E/S0s, which account for many of the spheroid-dominated galaxies embedded in the main $FSMGR_{LT}$–M_{HI}/M_* locus in Figure 9. Based on a variety of evidence, including identification of temporal sequences in a "fueling diagram" linking stellar populations and

gas content, we have argued elsewhere that blue-sequence E/S0s reflect a process of gas-rich merger-induced bulge building followed by disk regrowth, which may play a crucial role in the morphological evolution of disk galaxies (KGB; W10a; Wei et al. 2010b; Moffett et al. 2012; S13). Other authors have also documented a "living" population of E/S0s (e.g., Driver et al. 2007; Cortese & Hughes 2009; Thilker et al. 2010; Huertas-Company et al. 2010; Marino et al. 2011). In the mass regime below the threshold scale, blue-sequence E/S0s overlap with BCDs, suggesting a continuity of phenomena; such galaxies are most common below the threshold scale, with a tapering population up to the bimodality scale.

While bursty star formation has traditionally been ascribed to dwarf galaxies, Kauffmann et al. (2006) demonstrate that stochastic star formation is in fact most prevalent for galaxies with the intermediate masses and surface mass densities of bulged spirals (which happen to coincide with those of blue-sequence E/S0s; KGB). From a comparison to semi-analytic models, these authors infer that the observed stochasticity reflects efficient processing of fresh gas infall. Ferreras et al. (2004) advance similar ideas in their analysis of intermediate-redshift galaxies, concluding that efficient, short-lived bursts are typical for galaxy rotation velocities $V \gtrsim 140$ km s^{-1}. These authors' bursty accretion picture is roughly consistent with ours, with the caveat that we emphasize the roles of not only cosmic infall but also gas processing mechanisms in refueling. The fundamental importance of both is illustrated by an "exception that proves the rule": the gas-dominated S0 at $V \sim 90$ km s^{-1} and $M_{HI}/M_* \sim 4$ in Figure 7(a) is UGC 9562, a polar ring galaxy for which the misalignment of fresh accretion relative to the inner bulge/disk orientation likely inhibits normal gas transport, creating a system hovering between the accretion-dominated and processing-dominated regimes.[24]

Both externally driven and secular gas inflow mechanisms should become more important above the threshold scale. Hopkins et al. (2010) perform an analytic timescale analysis comparing growth by cosmic accretion, merging, and secular disk evolution as a function of galaxy mass at $z = 0$. They find that although merger rates are insignificant compared to gas accretion rates for $M_{bary} \lesssim 10^{10} M_\odot$, the two become comparable at intermediate masses, as the merger rate (per Gyr) increases with galaxy mass (e.g., Maller et al. 2006). Furthermore, Sinha & Holley-Bockelmann (2012) find that the flyby interaction rate, normally ignored in theoretical merger histories, may exceed the minor merger rate at intermediate-mass scales. At these mass scales Hopkins et al. also find that reduced accretion enables secular processes such as bar formation to become relatively more important. Observationally, bars appear more common in lower-mass, later-type galaxies than in Sa–Sc galaxies (Barazza et al. 2008; Nair & Abraham 2010), but Ellison et al. (2011) argue that strong bars in galaxies with $M_* > 10^{10} M_\odot$ may be substantially more *effective* in enhancing star formation than bars in lower-mass galaxies (although the possibility of differential time lags in enhanced star formation complicates interpretation). On the other hand, central star formation enhancements strong enough to create blue-centered color gradients do not obviously correlate with the presence of

---

[24] Cox et al. (2001) make the case that the gas in this polar ring was accreted long before the galaxy's interaction with a neighbor. Independent evidence linking other polar rings to cosmic gas accretion includes low gas-phase metallicity (Spavone et al. 2010) and alignment within a large-scale cosmic wall (Stanonik et al. 2009).

bars, but instead with signs of minor mergers and interactions (Kannappan et al. 2004; Gonzalez-Perez et al. 2011; S13).

While morphology correlates better with FSMGR or U–NIR color[25] than with mass (compare Figures 11(a) and 12(b); see also Franx et al. 2008), the definition of the processing-dominated regime by morphology and/or U–NIR color is complicated by the variety of transitional states. The histograms in Figures 12(b)–(d) show three possible definitions, with only the most inclusive ((d): all bulged disks + bluish spheroid-dominated galaxies + reddish quasi-bulgeless galaxies) yielding a numerically dominant population between the threshold and bimodality scales, where intermediate gas-richness systems are the norm (Figure 12(a)). At the red end, this population includes residually star-forming S0s and dying spirals (Figure 11(a)), not unreasonably since such galaxies appear to extend the gas–star formation relation of "normal" Sa–Sc spirals in Figure 8. On the other hand, this analysis suggests that such "normal" spirals, although broad in their mass distribution, are not actually typical at any mass.

4.4.4. The Quenched Regime

Most galaxies in the quenched regime have negligible M_{gas}/M_*, although values of $FSMGR_{LT}$ as high as ~ 0.1 Gyr^{-1} are not uncommon. The low gas-to-stellar mass ratios in this regime may reflect not only slowed cosmic accretion but also ram-pressure stripping and/or efficient AGN feedback in hot-gas-dominated halos (e.g., Somerville et al. 2008; Woo et al. 2013). However, significant growth largely uncorrelated with cosmic gas accretion may be possible via intermittent satellite mergers, which might rejuvenate the galaxy either by briefly fueling star formation or by injecting stellar mass formed relatively recently in the satellite (Morganti et al. 2006; Martini et al. 2013). For spheroid-dominated galaxies, Martig et al. (2009) argue that "morphological quenching" inhibits the gas processing necessary to form stars, and indeed, the most massive ($V \gtrsim 325$ km s^{-1}) early-type galaxies seem to lack recent star formation regardless of gas content (Serra et al. 2008). Consistent with this idea, we see two degrees of quenching in Figure 11(a), with a distinct population of *nearly* quenched bulged disks forming a peak just blueward of the red-and-dead peak for spheroid-dominated galaxies. Arguably, these systems represent the extreme tail of the processing-dominated regime, appearing as dying spirals or slightly blue S0s. Previous studies have shown that residual star formation is common for S0s over a wide range in mass (e.g., Salim & Rich 2010; Moffett et al. 2012), even in environments where Es are quenched (Salim et al. 2012). Stellar mass loss might account for much of the gas supply (Sage & Welch 2006; Leitner & Kravtsov 2011). The phenomenon of partial quenching seen in Figure 11 reaffirms that both accretion and processing are important to refueling: although the hot gas in galaxy clusters greatly slows accretion (and also removes gas by ram-pressure stripping), still gas buildup can occur, and disk galaxies remain capable of processing it.

5. SUMMARY AND CONCLUSIONS

Our analysis has made use of two samples, both broadly representative of the general galaxy population down to the "high-mass dwarf" regime (baryonic masses $\sim 10^9$ $M_\odot$). These

samples span a wide range of void to cluster environments, with non-cluster galaxies naturally predominant. The NFGS comprises ~ 200 galaxies with newly complete H I data, partial CO data, and internal kinematic data homogenized from a mix of stellar, ionized gas, and neutral gas measurements. The NFGS H I database is uniquely powerful in providing detections or strong upper limits ($M_{H\,I} \lesssim 0.1 M_*$) for all galaxies. The V3000 sample comprises ~ 3000 galaxies in a volume-limited union of the SDSS and the blind 21 cm ALFALFA survey, with H I upper limits computed for all ALFALFA non-detections. We have combined SDSS and ALFALFA redshifts with redshifts from several other surveys to achieve high completeness in the V3000 sample down to baryonic masses $\sim 10^{9.3}$ $M_\odot$, although residual incompleteness for dwarf galaxies remains.

Using these data sets, we have confirmed and clarified observed shifts in gas-richness and morphology at two key galaxy mass scales.

1. Below the *gas-richness threshold scale* ($V \sim 125$ km s^{-1}; baryonic mass $\sim 10^{9.9}$ $M_\odot$), gas-dominated quasi-bulgeless disks become most numerous in the galaxy population.
2. Above the *bimodality scale* ($V \sim 200$ km s^{-1}; baryonic mass $\sim 10^{10.6}$ $M_\odot$), gas-starved spheroid-dominated galaxies rise to prominence, with numbers comparable to nearly quenched bulged disks.

Notwithstanding these transitions, we have shown that both of our samples display far greater scatter in M_{gas}/M_* as a function of V (a non-covariant mass proxy) than has been commonly assumed. In particular, the NFGS reveals the natural diversity of gas-richness in a sample unbiased with respect to 21 cm flux: its M_{gas}/M_* versus V plot is striking in its complexity, with quenched galaxies at all masses and scatter $\gtrsim 0.5$ dex even for unquenched galaxies. We suggest that the diversity of M_{gas}/M_* has been suppressed in previous studies by selection and detection biases, as well as the practice of plotting M_{gas}/M_* versus M_*, which allows large covariant errors in M_* to enhance the apparent correlation.

In contrast to its complicated correlation with mass, M_{gas}/M_* shows a simple and clean correlation with another fundamental quantity: the *long-term* fractional stellar mass growth rate ($FSMGR_{LT}$), which we define as the ratio of a galaxy's stellar mass formed within the last Gyr to its preexisting stellar mass. The M_{gas}/M_*–$FSMGR_{LT}$ correlation represents the physical underpinnings of the remarkably tight ($\sigma \sim 0.3$ dex) correlation between M_{gas}/M_* and U–NIR color, used in the "photometric gas fraction" technique of K04, because U–NIR color directly predicts $FSMGR_{LT}$. Importantly, a fractional growth rate is related to, but distinct from, an SSFR, as it can exceed a value of one over the unit of time. Choosing Gyr as our unit of time reveals the remarkable fact that for an unquenched galaxy, the mass of new stars formed in the last Gyr is roughly *equal to* the mass of fresh gas it has available for future star formation, within factors of a few. Thus, for galaxies, past performance is a predictor of future success. We have demonstrated that this result is incompatible with any reasonable closed box model and does not derive from the inherently short-term "gas fuels star formation" physics of the Kennicutt–Schmidt Law, contrary to previous interpretations of the photometric gas fraction technique. Instead, we have argued that it reflects the physics of refueling: both cosmic accretion and the mechanisms that drive internal gas processing must be routine on $\lesssim 1$ Gyr timescales.

We have distinguished three refueling regimes, described as follows.

---

[25] Interestingly, the bimodality in μ_Δ as a function of $(u - J)^e$ is much less apparent as a function of $FSMGR_{LT}$. We suspect that the coarse binning of possible $FSMGR_{LT}$ values in our stellar population models blurs the structure seen in $(u - J)^e$.

1. Blue quasi-bulgeless galaxies are *accretion-dominated*, enjoying largely continuous refueling and stellar mass growth of order 100% per Gyr. Contrary to their reputation for "inefficient" star formation, such gas-dominated dwarf galaxies appear to be growing exponentially. We suggest that their high M_{gas}/M_* ratios may be more fairly interpreted as evidence that they are "overwhelmed" rather than "inefficient."

2. Bulged disk galaxies are *processing-dominated*, consuming a reduced rate of fresh accretion in efficient, often externally driven bursts with net growth rates at tens of percentage levels. Mergers and interactions in this regime create fluctuations in morphology and gas content, including transient blue E/S0 states that may regenerate spiral morphology.

3. Red-and-dead spheroid-dominated galaxies are *quenched* (per the usual terminology), with negligible gas and $\sim$1%–10% stellar mass growth per Gyr. They may grow slowly by satellite accretion. A population of "nearly quenched" bulged disk galaxies lies at the interface of the processing-dominated and quenched regimes, extending the M_{gas}/M_*–FSMGR$_{LT}$ relation to low levels.

High SSFRs in dwarf galaxies are sometimes discounted as evidence of bursty star formation, which should average out to lower levels over time. We cannot rule out the possibility of an extremely high mass-to-light ratio, low-SSFR population missed in the V3000 sample due to incompleteness in the SDSS redshift survey. However, we note that FSMGR$_{LT}$ is averaged over the past Gyr. Moreover, we have reviewed evidence from recent studies suggesting that dwarf galaxies are *not* especially bursty, except for the major bursts obviously inherent in dwarf-dwarf mergers, such as might produce BCDs. In fact, we have argued that bulged disk galaxies are far more subject to bursty star formation than typical quasi-bulgeless dwarfs. As discussed, the burstiness of such processing-dominated galaxies likely reflects increasingly efficient mechanisms of gas processing (both gas transport and H I-to-H$_2$ conversion) that develop in tandem with, and partly because of, reduced cosmic accretion.

Connecting back to the threshold and bimodality scales, we have seen that the mass distributions of accretion-dominated, processing-dominated, and quenched galaxies cross at these two scales, suggesting an indirect relationship between refueling and galaxy mass. Focusing on galaxies that are central in their halos, we find a plausible correspondence between these galaxy mass scales and two halo mass scales previously linked to transitions in cosmic accretion ($\sim$10$^{11.5}$ and $\sim$10$^{12.1}$ $M_\odot$). In future work considering environment data we will examine the behavior of centrals and satellites separately, demonstrating that centrals evolve through the processing-dominated regime in precisely the narrow mass range between the threshold and bimodality scales. In fact, the V3000 sample demonstrates that "normal" galaxies like our Milky Way—bulged disks with intermediate gas richness—are not in general typical, but most nearly approach typical in this mass range.

Although the analysis in this paper has not used halo mass data, our results clearly motivate the need for a full analysis of M_{gas}/M_* versus V as a function of halo mass and central versus satellite status, for a sample that is highly complete down to galaxy masses below the threshold scale. To date no such sample exists, in that all surveys that probe the full diversity of galaxy environments lack sufficiently sensitive 21 cm data to probe the full range of M_{gas}/M_* in the dwarf regime. The NFGS offers a glimpse of the power of truly unbiased H I observations for a broad sample but lacks well-characterized and

fairly sampled environments, leading us back to the need for a volume-limited sample with high-quality 21 cm and kinematic data for a cosmologically diverse range of environments. We aim to construct such a data set as part of the RESOLVE Survey (http://resolve.astro.unc.edu), currently in progress on the SOAR, SALT, Gemini, GBT, and Arecibo telescopes.

Laboratory, Max Planck Institute for Astrophysics, New Mexico State University, New York University, Ohio State University, Pennsylvania State University, University of Portsmouth, Princeton University, the Spanish Participation Group, University of Tokyo, University of Utah, Vanderbilt University, University of Virginia, University of Washington, and Yale University.

REFERENCES

Abadi, M. G., Navarro, J. F., Steinmetz, M., & Eke, V. R. 2003, ApJ, 591, 499
Abazajian, K., Adelman-McCarthy, J. K., Agüeros, M. A., et al. 2004, AJ, 128, 502
Abazajian, K. N., Adelman-McCarthy, J. K., Agüeros, M. A., et al. 2009, ApJS, 182, 543
Adelman-McCarthy, J. K., Agueros, M. A., Allam, S. S., et al. 2008, ApJS, 175, 297
Aihara, H., Allende Prieto, C., An, D., et al. 2011, ApJS, 193, 29
Baldry, I. K., Glazebrook, K., Brinkmann, J., et al. 2004, ApJ, 600, 681
Barazza, F. D., Jogee, S., & Marinova, I. 2008, ApJ, 675, 1194
Barton, E. J., Kannappan, S. J., Kurtz, M. J., & Geller, M. J. 2000, PASP, 112, 367
Barway, S., Kembhavi, A., Wadadekar, Y., Ravikumar, C. D., & Mayya, Y. D. 2007, ApJL, 661, L37
Barway, S., Wadadekar, Y., Kembhavi, A. K., & Mayya, Y. D. 2009, MNRAS, 394, 1991
Begum, A., Chengalur, J. N., Karachentsev, I. D., & Sharina, M. E. 2008, MNRAS, 386, 138
Behroozi, P. S., Wechsler, R. H., & Conroy, C. 2013, ApJ, 770, 57
Bekki, K. 2008, MNRAS, 388, L10
Bell, E. F. 2008, ApJ, 682, 355
Bell, E. F., McIntosh, D. H., Katz, N., & Weinberg, M. D. 2003, ApJS, 149, 289
Bettoni, D., Galletta, G., & García-Burillo, S. 2003, A&A, 405, 5
Bigiel, F., Leroy, A., Walter, F., et al. 2008, AJ, 136, 2846
Birnboim, Y., & Dekel, A. 2003, MNRAS, 345, 349
Blanton, M. R., Kazin, E., Muna, D., Weaver, B. A., & Price-Whelan, A. 2011, AJ, 142, 31
Blanton, M. R., & Roweis, S. 2007, AJ, 133, 734
Blitz, L., & Rosolowsky, E. 2006, ApJ, 650, 933
Bouché, N., Dekel, A., Genzel, R., et al. 2010, ApJ, 718, 1001
Brooks, A. M., Governato, F., Booth, C. M., et al. 2007, ApJL, 655, L17
Bruzual, G., & Charlot, S. 2003, MNRAS, 344, 1000
Bundy, K., Ellis, R. S., & Conselice, C. J. 2005, ApJ, 625, 621
Burstein, D., Bender, R., Faber, S., & Nolthenius, R. 1997, AJ, 114, 1365
Calzetti, D. 2001, PASP, 113, 1449
Cardelli, J. A., Clayton, G. C., & Mathis, J. S. 1989, ApJ, 345, 245
Catinella, B., Schiminovich, D., Kauffmann, G., et al. 2010, MNRAS, 403, 683
Churchill, C. W., Kacprzak, G. G., Steidel, C. C., et al. 2012, ApJ, 760, 68
Colless, M., Peterson, B. A., Jackson, C., et al. 2003, arXiv:astro-ph/0306581
Cortese, L., & Hughes, T. M. 2009, MNRAS, 400, 1225
Cox, A. L., Sparke, L. S., Watson, A. M., & van Moorsel, G. 2001, AJ, 121, 692
Dalcanton, J. J. 2007, ApJ, 658, 941
Dalcanton, J. J., Yoachim, P., & Bernstein, R. A. 2004, ApJ, 608, 189
Davé, R., Finlator, K., & Oppenheimer, B. D. 2012, MNRAS, 421, 98
Davé, R., Katz, N., Oppenheimer, B. D., Kollmeier, J. A., & Weinberg, D. H. 2013, MNRAS, 434, 2645
Davies, R. L., Efstathiou, G., Fall, S. M., Illingworth, G., & Schechter, P. L. 1983, ApJ, 266, 41
Dekel, A., & Birnboim, Y. 2006, MNRAS, 368, 2
Dekel, A., & Silk, J. 1986, ApJ, 303, 39
D'Onghia, E., & Burkert, A. 2004, ApJL, 612, L13
Driver, S. P., Allen, P. D., Liske, J., & Graham, A. W. 2007, ApJL, 657, L85
Driver, S. P., Hill, D. T., Kelvin, L. S., et al. 2011, MNRAS, 413, 971
Ellison, S. L., Nair, P., Patton, D. R., et al. 2011, MNRAS, 416, 2182
Emsellem, E., Cappellari, M., Krajnović, D., et al. 2007, MNRAS, 379, 401
Falco, E. E., Kurtz, M. J., Geller, M. J., et al. 1999, PASP, 111, 438
Ferreras, I., Silk, J., Böhm, A., & Ziegler, B. 2004, MNRAS, 355, 64
Feulner, G., Goranova, Y., Drory, N., Hopp, U., & Bender, R. 2005, MNRAS, 358, L1
Fisher, D. B., & Drory, N. 2011, ApJL, 733, L47
Fontanot, F., De Lucia, G., Wilman, D., & Monaco, P. 2011, MNRAS, 416, 409
Franx, M., van Dokkum, P. G., Schreiber, N. M. F., et al. 2008, ApJ, 688, 770
Fraternali, F., & Tomassetti, M. 2012, MNRAS, 426, 2166
Gardan, E., Braine, J., Schuster, K. F., Brouillet, N., & Sievers, A. 2007, A&A, 473, 91

Garnett, D. R. 2002, ApJ, 581, 1019
Geha, M., Blanton, M., Yan, R., & Tinker, J. 2012, ApJ, 757, 85
Giavalisco, M., Vanzella, E., Salimbeni, S., et al. 2011, ApJ, 743, 95
Giovanelli, R., Haynes, M. P., Kent, B. R., et al. 2005, AJ, 130, 2598
Giovanelli, R., Haynes, M. P., Salzer, J. J., et al. 1994, AJ, 107, 2036
Gonzalez-Perez, V., Castander, F. J., & Kauffmann, G. 2011, MNRAS, 411, 1151
Governato, F., Willman, B., Mayer, L., et al. 2007, MNRAS, 374, 1479
Hawarden, T. G., Longmore, A. J., Goss, W. M., Mebold, U., & Tritton, S. B. 1981, MNRAS, 196, 175
Haynes, M. P., & Giovanelli, R. 1984, AJ, 89, 758
Haynes, M. P., Giovanelli, R., Martin, A. M., et al. 2011, AJ, 142, 170
Hopkins, P. F., Kereš, D., Ma, C.-P., & Quataert, E. 2010, MNRAS, 401, 1131
Hopkins, P. F., Somerville, R. S., Cox, T. J., et al. 2009, MNRAS, 397, 802
Huang, S., Haynes, M. P., Giovanelli, R., & Brinchmann, J. 2012, ApJ, 756, 113
Huchra, J., Davis, M., Latham, D., & Tonry, J. 1983, ApJS, 52, 89
Huertas-Company, M., Aguerri, J. A. L., Tresse, L., et al. 2010, A&A, 515, A3
Isobe, T., Feigelson, E. D., & Nelson, P. I. 1986, ApJ, 306, 490
Jansen, R. A., Fabricant, D., Franx, M., & Caldwell, N. 2000a, ApJS, 126, 331
Jansen, R. A., Franx, M., Fabricant, D., & Caldwell, N. 2000b, ApJS, 126, 271
Jarrett, T. H., Chester, T., Cutri, R., et al. 2000, AJ, 119, 2498
Jones, D. H., Read, M. A., Saunders, W., et al. 2009, MNRAS, 399, 683
Kannappan, S. J. 2004, ApJL, 611, L89 (K04)
Kannappan, S. J., & Barton, E. J. 2004, AJ, 127, 2694
Kannappan, S. J., & Fabricant, D. G. 2001, AJ, 121, 140
Kannappan, S. J., Fabricant, D. G., & Franx, M. 2002, AJ, 123, 2358 (KFF)
Kannappan, S. J., & Gawiser, E. 2007, ApJL, 657, L5
Kannappan, S. J., Guie, J. M., & Baker, A. J. 2009, AJ, 138, 579 (KGB)
Kannappan, S. J., Jansen, R. A., & Barton, E. J. 2004, AJ, 127, 1371
Kannappan, S. J., & Wei, L. H. 2008, in AIP Conf. Proc. 1035, The Evolution of Galaxies through the Neutral Hydrogen Window, ed. R. Minchin & E. Momjian (Melville, NY: AIP), 163
Kassin, S. A., Weiner, B. J., Faber, S. M., et al. 2007, ApJL, 660, L35
Kauffmann, G., Heckman, T. M., De Lucia, G., et al. 2006, MNRAS, 367, 1394
Kauffmann, G., Heckman, T. M., White, S. D. M., et al. 2003a, MNRAS, 341, 54
Kauffmann, G., Heckman, T. M., White, S. D. M., et al. 2003b, MNRAS, 341, 33
Kereš, D., Katz, N., Weinberg, D. H., & Davé, R. 2005, MNRAS, 363, 2
Khochfar, S., & Silk, J. 2011, MNRAS, 410, L42
Krumholz, M. R., & Dekel, A. 2012, ApJ, 753, 16
Krumholz, M. R., Leroy, A. K., & McKee, C. F. 2011, ApJ, 731, 25
Kurtz, M. J., Mink, D. J., Wyatt, W. F., et al. 1992, in ASP Conf. Ser. 25, Astronomical Data Analysis Software and Systems I, ed. D. M. Worrall, C. Biemesderfer, & J. Barnes (San Francisco, CA: ASP), 432
La Barbera, F., De Carvalho, R. R., De La Rosa, I. G., et al. 2010, AJ, 140, 1528
Laurikainen, E., Salo, H., Buta, R., Knapen, J. H., & Comerón, S. 2010, MNRAS, 405, 1089
Lavalley, M. P., Isobe, T., & Feigelson, E. D. 1992, BAAS, 24, 839
Leaman, R., Cole, A. A., Venn, K. A., et al. 2009, ApJ, 699, 1
Leaman, R., Venn, K. A., Brooks, A. M., et al. 2012, ApJ, 750, 33
Leauthaud, A., Tinker, J., Bundy, K., et al. 2012, ApJ, 744, 159
Lee, J. C., Gil de Paz, A., Kennicutt, R. C., Jr., et al. 2011, ApJS, 192, 6
Lee, J. C., Kennicutt, R. C., Jr., Funes, S. J. J. G., Sakai, S., & Akiyama, S. 2009, ApJ, 692, 1305
Leitner, S. N., & Kravtsov, A. V. 2011, ApJ, 734, 48
Li, C., Kauffmann, G., Fu, J., et al. 2012, MNRAS, 424, 1471
Lu, Y., Kereš, D., Katz, N., et al. 2011, MNRAS, 416, 660
Mac Low, M., & Ferrara, A. 1999, ApJ, 513, 142
Madden, S. C., Poglitsch, A., Geis, N., Stacey, G. J., & Townes, C. H. 1997, ApJ, 483, 200
Maller, A. H., Katz, N., Kereš, D., Davé, R., & Weinberg, D. H. 2006, ApJ, 647, 763
Marino, A., Bianchi, L., Rampazzo, R., et al. 2011, ApJ, 736, 154
Martig, M., Bournaud, F., Teyssier, R., & Dekel, A. 2009, ApJ, 707, 250
Martin, A. M., Papastergis, E., Giovanelli, R., et al. 2010, ApJ, 723, 1359
Martin, C. L., Shapley, A. E., Coil, A. L., et al. 2012, ApJ, 760, 127
Martini, P., Dicken, D., & Storchi-Bergmann, T. 2013, ApJ, 766, 121
Mazzarella, J. M., & Boroson, T. A. 1993, ApJS, 85, 27
McGaugh, S. S. 2005, ApJ, 632, 859
McGaugh, S. S., Schombert, J. M., Bothun, G. D., & de Blok, W. J. G. 2000, ApJL, 533, L99
Misgeld, I., & Hilker, M. 2011, MNRAS, 414, 3699
Moffett, A. J., Kannappan, S. J., Baker, A. J., & Laine, S. 2012, ApJ, 745, 34

Morganti, R., de Zeeuw, P. T., Oosterloo, T. A., et al. 2006, MNRAS, 371, 157
Morrissey, P., Conrow, T., Barlow, T. A., et al. 2007, ApJS, 173, 682
Moster, B. P., Naab, T., & White, S. D. M. 2013, MNRAS, 428, 3121
Mulchaey, J. S., & Jeltema, T. E. 2010, ApJL, 715, L1
Nair, P. B., & Abraham, R. G. 2010, ApJL, 714, L260
Narayanan, A., Wakker, B. P., Savage, B. D., et al. 2010, ApJ, 721, 960
Navarro, J. F., & White, S. D. M. 1994, MNRAS, 267, 401
Nelson, D., Vogelsberger, M., Genel, S., et al. 2013, MNRAS, 429, 3353
O'Donnell, J. E. 1994, ApJ, 422, 158
Papastergis, E., Martin, A. M., Giovanelli, R., & Haynes, M. P. 2011, ApJ, 739, 38
Paturel, G., Petit, C., Prugniel, P., et al. 2003, A&A, 412, 45
Pelupessy, F. I., & Papadopoulos, P. P. 2009, ApJ, 707, 954
Peng, Y.-j., Lilly, S. J., Renzini, A., & Carollo, M. 2012, ApJ, 757, 4
Pfenniger, D., & Revaz, Y. 2005, A&A, 431, 511
Pisano, D. J., Kobulnicky, H. A., Guzmán, R., Gallego, J., & Bershady, M. A. 2001, AJ, 122, 1194
Pustilnik, S. A., Kniazev, A. Y., Lipovetsky, V. A., & Ugryumov, A. V. 2001, A&A, 373, 24
Raychaudhury, S., von Braun, K., Bernstein, G. M., & Guhathakurta, P. 1997, AJ, 113, 2046
Reyes, R., Mandelbaum, R., Gunn, J. E., et al. 2012, MNRAS, 425, 2610
Robertson, B., Bullock, J. S., Cox, T. J., et al. 2006, ApJ, 645, 986
Sage, L. J., & Welch, G. A. 2006, ApJ, 644, 850
Salim, S., Dickinson, M., Michael Rich, R., et al. 2009, ApJ, 700, 161
Salim, S., Fang, J. J., Rich, R. M., Faber, S. M., & Thilker, D. A. 2012, ApJ, 755, 105
Salim, S., & Rich, R. M. 2010, ApJL, 714, L290
Salim, S., Rich, R. M., Charlot, S., et al. 2007, ApJS, 173, 267 (S07)
Sancisi, R., Fraternali, F., Oosterloo, T., & van der Hulst, T. 2008, A&ARv, 15, 189
Schawinski, K., Lintott, C., Thomas, D., et al. 2009, MNRAS, 396, 818
Schawinski, K., Urry, C. M., Virani, S., et al. 2010, ApJ, 711, 284
Schlegel, D. J., Finkbeiner, D. P., & Davis, M. 1998, ApJ, 500, 525
Schruba, A., Leroy, A. K., Walter, F., et al. 2011, AJ, 142, 37
Serra, P., Trager, S. C., Oosterloo, T. A., & Morganti, R. 2008, A&A, 483, 57
Sheth, K., Regan, M., Hinz, J. L., et al. 2010, PASP, 122, 1397
Sinha, M., & Holley-Bockelmann, K. 2012, ApJ, 751, 17
Somerville, R. S., Hopkins, P. F., Cox, T. J., Robertson, B. E., & Hernquist, L. 2008, MNRAS, 391, 481
Spavone, M., Iodice, E., Arnaboldi, M., et al. 2010, ApJ, 714, 1081
Stanonik, K., Platen, E., Aragón-Calvo, M. A., et al. 2009, ApJL, 696, L6
Stark, D. V., Kannappan, S. J., Wei, L. H., et al. 2013, ApJ, 769, 82 (S13)
Stewart, K. R. 2011, arXiv:1109.3207
Stewart, K. R., Bullock, J. S., Wechsler, R. H., & Maller, A. H. 2009, ApJ, 702, 307
Stewart, K. R., Bullock, J. S., Wechsler, R. H., Maller, A. H., & Zentner, A. R. 2008, ApJ, 683, 597
Stewart, K. R., Kaufmann, T., Bullock, J. S., et al. 2011, ApJ, 738, 39
Thilker, D. A., Bianchi, L., Schiminovich, D., et al. 2010, ApJL, 714, L171
Tremonti, C. A., Heckman, T. M., Kauffmann, G., et al. 2004, ApJ, 613, 898
van den Bergh, S. 1976, ApJ, 206, 883
van der Marel, R. P., & Franx, M. 1993, ApJ, 407, 525
van de Voort, F., Schaye, J., Booth, C. M., Haas, M. R., & Dalla Vecchia, C. 2011, MNRAS, 414, 2458
Wei, L. H., Kannappan, S. J., Vogel, S. N., & Baker, A. J. 2010a, ApJ, 708, 841 (W10a)
Wei, L. H., Vogel, S. N., Kannappan, S. J., et al. 2010b, ApJL, 725, L62
Weil, M. L., Eke, V. R., & Efstathiou, G. 1998, MNRAS, 300, 773
Weinzirl, T., Jogee, S., Khochfar, S., Burkert, A., & Kormendy, J. 2009, ApJ, 696, 411
Weisz, D. R., Johnson, B. D., Johnson, L. C., et al. 2012, ApJ, 744, 44
Woo, J., Dekel, A., Faber, S. M., et al. 2013, MNRAS, 428, 3306
Yoachim, P., & Dalcanton, J. J. 2005, ApJ, 624, 701
Zhang, W., Li, C., Kauffmann, G., et al. 2009, MNRAS, 397, 1243
Zitrin, A., & Brosch, N. 2008, MNRAS, 390, 408